MECHANICAL PROPERTIES OF A NEW HIGH SPECIFIC STRENGTH HONEYCOMB FROM AMORPHOUS METAL

By

BALAJI JAYAKUMAR

Bachelor of Engineering in Aeronautical Engineering
Park College of Engineering and Technology
Affiliated to Anna University
Tamil Nadu, India
2006

Master of Science in Mechanical and Aerospace Engineering
Oklahoma State University
Stillwater, OK
2009

Submitted to the Faculty of the
Graduate College of the
Oklahoma State University
in partial fulfillment of
the requirements for
the Degree of
DOCTOR OF PHILOSOPHY
May, 2015

MECHANICAL PROPERTIES OF A NEW HIGH SPECIFIC STRENGTH HONEYCOMB FROM AMORPHOUS METAL

Dissertation Approved:

Dr. Jay C. Hanan

Dissertation Adviser

Dr. Sandip P. Harimkar

Dr. James M. Manimala

Dr. Ranji K. Vaidyanathan

ACKNOWLEDGEMENTS

The Oklahoma Center for Advancement and Technology- Oklahoma Applied Research Support (OCAST-OARS Award Nos. AR12.-041, AR 131-037) and the National Science Foundation (NSF Award No: 1214985) partially funded this work at MetCel LLC and the Helmerich Research Center through grants to the OSU Foundation. Welding work was performed at Edison Welding Institute (EWI), OH in collaboration with research support from MetCel LLC.

Acknowledgements reflect the views of the author and are not endorsed by committee members or Oklahoma State University.

Name: BALAJI JAYAKUMAR

Date of Degree: MAY, 2015

Title of Study: MECHANICAL PROPERTIES OF A NEW HIGH SPECIFIC STRENGTH HONEYCOMB FROM AMORPHOUS METAL

Major Field: MECHANICAL AND AEROSPACE ENGINEERING

Abstract: Using metallic glasses as base materials, Amorphous Metal Honeycombs (AMHs) with a teardrop cellular geometry were manufactured. A new analytical model was proposed to predict the relative density and axial compressive strength of teardrop celled AMHs. Using this, an optimum theoretical density at which axial compressive strength of AMHs exceed theoretical strengths of aluminum honeycombs were predicted. Results from experimental testing of AMHs in the density range of 0.3 Mg/m^3 to 0.6 Mg/m^3 validate the proposed analytical model. AMH with a density of 0.6 Mg/m^3 and cell size of 1.1 mm showed a higher axial compressive strength compared to aluminum honeycombs. The proposed model also shows that a higher maximum yield stress is achievable by improving inter-cellular bonding. A successful welding method has been demonstrated to join amorphous $Fe_{45}Ni_{45}Mo_7B_3$ ribbons at a higher cooling rate. XRD studies on welded samples from this method do not show crystallization. Ribbons remained amorphous before and after the weld. By improving the cooling rate of the weld, crystallization was avoided maintaining the strength of the weld. Using a method similar to peening, significant curvatures were observed in amorphous $Fe_{45}Ni_{45}Mo_7B_3$ ribbons. While the prediction of a tempering state would imply a residual compressive surface stress upon layer removal, peening of amorphous ribbons showed an opposite response. The amorphous phase of peened ribbons remained, as evident from XRD data. SEM micrographs show distorted ribbon edges and an average thickness reduction of 10% after peening also confirmed by X-ray transmission measurements. Young's modulus and yield strength measured from bulk tension testing of the in-plane direction did not show a significant change as a result of peening.

Table of Contents

LIST OF TABLES

LIST OF FIGURES

CHAPTER I

INTRODUCTION

1.1 Motivation

Honeycombs are cellular structures typically used as core materials in sandwich panels. Excellent mechanical and thermal properties have enabled their use in aerospace, ballistic protection, packaging and other similar applications. A high volume of honeycombs in sandwich panels are used in aerospace structures. In addition to wing structures and radomes, about 300 m^2 of honeycombs are used in floor panels on a commercial aircraft[1]. In a sandwich construction, the top and bottom face skins are separated by a light weight honeycomb core. This separation by the core increases buckling and bending resistance of the panel. It is important to maximize axial compressive strength of the core, to support structural loads. Compressive strength also enhances other properties such as bending, shear, and mechanical energy absorption. In a structural loading scenario, face sheets carry bending stresses and core carries shear stresses. There are applications, where axial compressive properties of honeycomb are as critical as shear properties.

[1]U.S. Patent No. 20090072086, Smith, L., Y. S. Wang, et al. "Aircraft Floor and Interior Panels Using Edge Coated Honeycomb." HexCel Corporation. (2009).

Especially, strength-to-weight ratio also known as specific strength is important for weight-sensitive applications. Both metallic and non-metallic base materials have been used in manufacturing honeycombs. Aluminum alloys, steel, resin coated paper, and Polyproplene are some examples. Ceramics have also been used in honeycomb form for catalytic convertors. In aircraft manufacturing, Aluminum and Nomex[2] are the most commonly used honeycombs. Their high specific strengths and varying range of manufacturable densities enabled their many uses. Hexagonal (the most common cell shape) honeycombs have anisotropic mechanical properties; that is different properties in the in-plane and out-of-plane directions. They are most effective when loaded in the out-of-plane (axial) direction. They are typically manufactured using expansion and corrugation methods in which materials are plastically deformed to form hexagonal cells. Inter-cellular bonding is achieved using adhesives or welding. Mechanical properties of base material and cellular geometry determine a honeycomb's structural performance. Stronger and stiffer base materials yield better performing honeycombs. Formability, practically achievable cell sizes and cell wall thicknesses are all critical in determining deformation mechanisms.

First discovered in 1960 [1], Amorphous alloys in the form of ribbons and wires were manufactured using rapid solidification processes at very high cooling rates of 10^4 - 10^6 K/s, restricting their sizes at least in one dimension. Amorphous metals (also known as Metallic Glasses- MGs) are non-crystalline materials. Their atomic structure is characterized by disorder and free volume, without crystal defects such as dislocations and grain boundaries. They have high Yield Strengths (up to 5 GPa [2]) and Young's modulus (up to 195 GPa [3]). The absence of grain boundaries also aids in corrosion resistance and

[2] Nomex is a meta-aramid material, registered trademark of DuPont Inc.

magnetic susceptibility. Early applications have been developed in drill bit coatings, magnetic sensors [4, 5], and transformer cores [6, 7]. Their magnetic and structural properties are controlled by alloy composition and thermo magnetic treatments. Recently, Bulk Metallic Glasses (BMGs) processed at lower cooling rates have been considered for structural applications because of their unique mechanical properties in bulk form. But, near-zero ductility in tension and limited plasticity in compression are considered their "Achilles heel" [8]. Recent work [8-11] has aimed at improving plasticity and toughness of MGs, also through the development of amorphous cellular solids [12]. Processing and characterization of Zr- and Pd- amorphous metal foams using different approaches have been studied and reported in literature [13-16]. Palladium based foams ($Pd_{43}Ni_{10}Cu_{27}P_{20}$) have been produced using thermoplastic foaming to 86% porosity and are capable of yielding at a high plastic strength of 250-600 MPa [15]. These were tested under a microgravity environment and considered for NASA space applications [17, 18]. Their behavior and underlying deformation physics have been studied [15, 19]. Realizing their application as a high mechanical energy storing material, micro-trusses using amorphous alloys have also been developed [20-22].

Control of porosity influences mechanical properties of cellular structures. Existing analytical models support this and show that for the same density of solid base material, honeycombs are 16 times stronger than foams [23]. For cellular materials designed for high strength, it is advantageous to make Amorphous Metal Honeycombs (AMH). High Yield strengths and Young's modulus of MGs makes them favorable candidates for use as honeycomb base materials. Their high elastic limit and corrosion resistance, allow them to compete even with Polymer Matrix Composites such as CFRPs and GFRPs. With

superior properties, AMH can be realized as a replacement of other heavier materials, opening up material options for a design engineer in weight reduction and performance enhancement in packaging, aerospace, ballistics and similar applications. For example, application of an early version of AMH in a Body Armor against a 7.62 mm rifle round has already shown improvements in ballistic performance[24]. Using suitable processing methods, AMH can be tailored to obtain a specific strength.

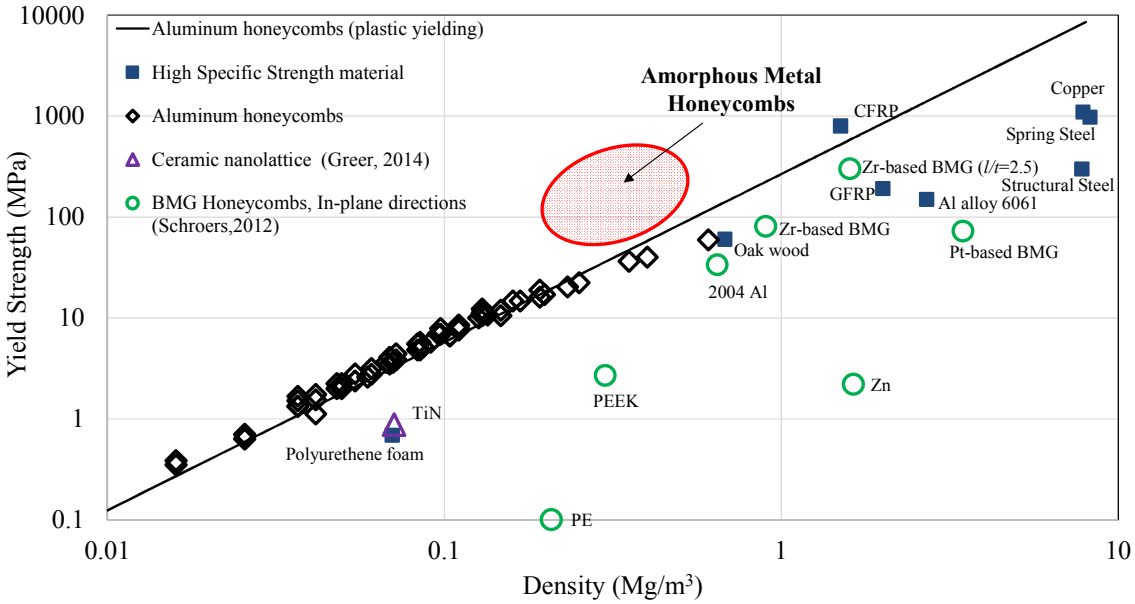

Figure 1 Density vs Yield Strength for high specific strength materials [25] compared to the highest specific strength aluminum honeycombs [26] , recently developed BMG honeycombs [27] and a ceramic nano-lattice [28]. Line represents theoretical prediction [23] and symbols are experimental data.

1.2 Research Gap

There is a need for lighter high strength materials for many applications. One solution is AMH. However, presently no method exists that is compatible with practical manufacturing methods. Thus, the need to design and develop scalable manufacturing methods for making honeycombs using MGs in tailored densities exists. Recent efforts have shown the possibility of high strength in Zr-, Pt- based BMG honeycombs [27] and Ti-N nano-lattices [28], but on a lab scale with significant limitations on scalability. MGs

show little to no plasticity. Deformation in MGs takes place as an on-set of shear bands, which act as defects. This limits honeycomb cell shapes. For example, the hexagonal cell shape has six plastic hinges in a given cell. MGs have high elastic limits; 2% (compared to 0.5% in crystalline materials). About 1% strain is required to form each hinge using MG precursors of 29 μm thickness. Because of this, the expansion method cannot be used in manufacture as it would cause the honeycomb to spring back. Shear bands are expected in hinges in each corner of a hexagonal cell. These shear bands act as defects potentially weakening the honeycomb across the cellular network, also making any method that involves corrugation undesirable for MGs. For these reasons, the common processes in manufacturing Aluminum and Nomex honeycombs cannot be used to produce AMH from precursor foils.

Recently, a new bottom-up manufacturing method was developed for AMH with a "teardrop" cell shape [24]. Amorphous $Fe_{45}Ni_{45}Mo_7B_3$ foils of 29 μm thickness were used in making honeycombs with a density of 0.3 Mg/m^3 up to a cross-section of 304 x 304 mm [29]. In this method, MG foils were folded and bonded using an adhesive to form cells. Designed for high compressive strength and energy absorption applications, AMH using different lab scale methods were manufactured and tested for mechanical properties in the axial direction. Results showed a significant difference in mechanical properties compared to accepted analytical models [23] for hexagonal honeycombs.

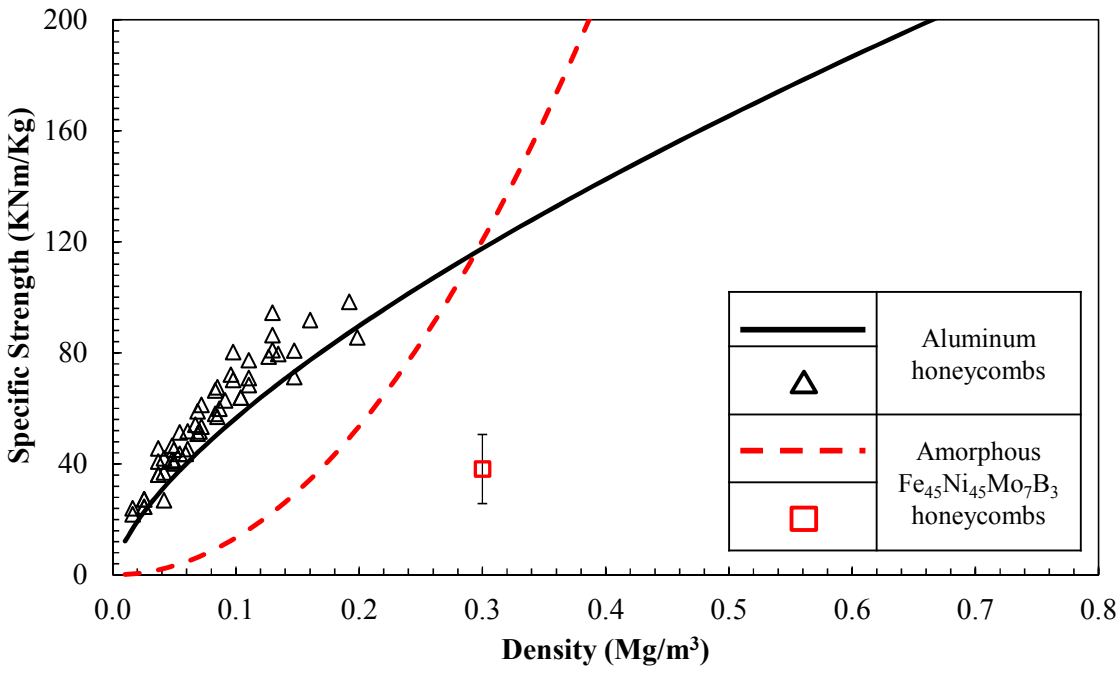

Figure 2 Lines represent theoretical predictions [23] for a hexagonal cell, symbols are experimental data, Experimental data for Aluminum honeycombs [30] , Amorphous $Fe_{45}Ni_{45}Mo_7B_3$ honeycombs [24, 31], error bars for AMH from std. dev. (No. of samples – 4)

This was mainly because

1. The prediction of specific strength was based on hexagonal cell and not "teardrop". Analytical models exist for hexagonal, circular, square and rectangular cells. A model for relative density and compression strength for a "teardrop" cell had not been developed.
2. Defects including bonding mismatch and cell wall misalignment from early prototypes affected mechanical properties. Defects have shown to influence honeycomb mechanical properties upto 40% [32].

Aluminum being the most widely used high specific strength metallic honeycomb, was considered the baseline for comparison. This comparison (Figure 2) shows a theoretical density at which AMH can exceed the specific strength of Aluminum Honeycombs. Due

to the reasons listed above, experimental values were well short of predictions. A more accurate model was required to predict an optimum design density beyond which AMH can have a higher specific strength than Aluminum honeycombs. A relative density model for a "teardrop" cell shape is required to predict resulting honeycomb densities. To predict axial specific strength, deformation mechanisms in the "out-of-plane" direction need to be modeled. In honeycomb compression, the ratio of wall thickness-to-cell size, the "*t/l*" ratio is a critical cell geometric parameter. Limited availability of MG ribbon thicknesses lead to targeting cell size *"l"* for a constant *"t"* to change honeycomb density. In designing a high specific strength honeycomb, a strong inter-cellular bond and minimal non-functional mass are critical. This makes welding an attractive bonding option, however avoiding cracks, crystallization and achieving a successful weld by retaining an amorphous structure in the ribbons are challenges. Other techniques that allow formation of a teardrop cell shape using thin foils are useful, as long as they help reduce the weight, and keep the manufacturing process efficient. Presented later, the use of residual stress in making "teardrop" shapes using amorphous $Fe_{45}Ni_{45}Mo_7B_3$ is a working example.

1.3 Objective

The ultimate goal of this work is to demonstrate Amorphous Metal Honeycombs of a higher specific strength compared to Aluminum honeycombs in the out-of-plane direction. Amorphous $Fe_{45}Ni_{45}Mo_7B_3$ precursors of 29 μm thickness were used in this study. Proposed processing methods include adhesive joining, welding, and a method similar to shot peening.

This dissertation is presented in 3 chapters. Each chapter provides a background of literature, materials and methods used in experimentation, discussion of results, and conclusions. Chapter 2 presents a closed form analytical solution for predicting the density and axial compressive strength of a "teardrop" celled honeycomb in the out-of-plane (X_3) direction. The proposed model was validated using experimental results from mechanical testing of amorphous $Fe_{45}Ni_{45}Mo_7B_3$ honeycombs using different honeycomb densities. A higher modulus amorphous metal (Nanosteel) was also tested and compared to validate the proposed model. Existing analytical models for hexagonal honeycombs, data published in scientific literature, and industry data sheets for Aluminum and Nomex honeycombs are compared and contrasted. Limitations of the model are also discussed.

While the bottom-up manufacturing approach [33] has several advantages, such as forming variable densities, minimizing stress concentrations, and weight savings from efficient design; it also presents a set of challenges. A critical one is mass addition from adhesive. Measurements from early AMH samples [29, 33] have shown up to 40% mass addition from adhesives. Inter-cellular bonding stabilizes the honeycomb cellular network and helps resist loading. Stronger inter-cellular bonding improves honeycomb performance both in shear and compression [34]. Minimizing mass from adhesive is critical also to improve specific strengths. A possible better option is to eliminate adhesives and weld inter-cellular nodes. Welding can also increase the honeycomb's functional service temperature. Typically corrugated stainless steel and Inconel alloy honeycombs are welded or brazed for high temperature applications up to 740 °C (1300 F). Welding amorphous metals has been considered in other applications. Particularly to overcome size constraints in BMGs. Welding has been a challenge due to MG's small window of time to

crystallization. *In order to study welding as a viable inter-cellular bonding method in AMH, welding feasibility of amorphous metals and their influence on their microstructure needs investigation.* Chapter 3 presents investigations on welding feasibility of Amorphous Metal Ribbons (AMR). A modified welding method and their influence on microstructure and inter-cellular bonding strength is presented.

In an attempt to reduce adhesives that add mass and welding that add cost and complexity, a new method of manufacturing AMH was envisioned from a lab discovery. When amorphous ribbons were shot peened, sizeable ribbon curvatures were observed. Responses were seen to change with peening conditions. The curvature was significant enough to resemble a "teardrop", cell shape of interest in this study. Due to the need for rapid quenching, residual stresses have been expected in amorphous metals. While prediction of a tempering state would imply a residual compressive surface stress, this peening method shows an opposite response. *Significant curvature obtained using the shot peening method suggests a change in the residual stress state.* Chapter 4 presents the studies on shot peening and residual stresses in $Fe_{45}Ni_{45}Mo_7B_3$ ribbons. The influence of peening on ribbon mechanical properties are also discussed.

CHAPTER II

ANALYTICAL MODELING OF AMORPHOUS METAL HONEYCOMBS

2.1 Background

The first accepted analytical model that predicts crushing behavior of a honeycomb with hexagonal cells, in the axial direction was presented by McFarland in 1963. Wierzbicki's correction to this model was published in 1983. Gibson and Ashby analyzed mechanical behavior of hexagonal honeycombs in the in-plane (X_1 and X_2) and out-of-plane (X_3) directions [35, 36].

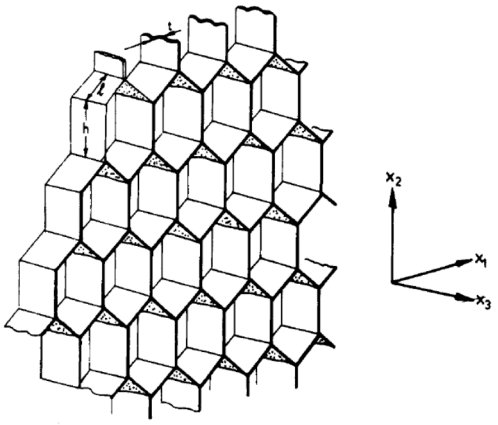

Figure 3 Hexagonal celled honeycombs, showing in-plane (X_1 and X_2) and out-of-plane (X_3) directions [23].

From existing models it is clear that, in all types of thin walled structures, compressive strength depends on cell wall thickness and cell size [37].

Compressive behavior of honeycombs under axial loading are well explained in earlier work [38, 39]. Buckling behavior of honeycomb unit cells with a range of geometries, their density, and specific peak stress have been reported [40].

Influences of defects and imperfections have shown to reduce the strength and modulus of honeycomb up to 40% [40-43]. Several empirical formulae predicting peak and plateau stress in quasi-static and dynamic loading conditions have been reported [44, 45]. Crush behavior of square celled thin walled structures have also been studied theoretically and numerically analyzed [46].

Out-of-plane properties of honeycombs with square, rectangle, and triangular cells have been studied elsewhere [47]. Earlier work presented the critical load of failure for hexagonal cellular structures [48]. Some corrections for bending and extensional deformation for this model was later proposed [49]. Following this, several studies were conducted on the deformation behavior of hexagonal cell structures in axial loading (X_3) direction [36, 50]. Empirical equations predict the compressive strength, $(\sigma_{el}^*)_3$, due to elastic buckling and due to plastic buckling $(\sigma_{pl}^*)_3$ in the out-of-plane, X_3, direction for different cell shapes [32, 37, 47, 51-53]. These all provide a rich background and examples of how new cell types can be studied.

2.2 Specific Aims

(1) Develop an analytical model to predict the relative density and compressive strength (σ_3^*) of a "teardrop" celled honeycomb.

(2) Predict and demonstrate an optimal design density beyond which the axial specific strength of AMH exceeds hexagonal celled Aluminum honeycombs.

(3) Experimentally validate the proposed model from experimental testing of AMH.

2.3 Proposed Model

2.3.1 Relative density

The properties of a honeycomb have their highest level of dependence on relative density—ratio of honeycomb density and density of solid material. For all honeycombs, the cell edge length l is greater than wall thickness t ($l>>t$). Relative density may be represented in the form,

$$\frac{\rho^*}{\rho_S} = C\left(\frac{t}{l}\right) \tag{1}$$

where t is cell wall thickness, l is cell size, and C is numerical constant that is dependent on details of cell shape [23]. An image of an amorphous $Fe_{45}Ni_{45}Mo_7B_3$ honeycomb cells with a "teardrop" cellular shape taken using Micro Computed Tomography is shown in Figure 4. Also shown is the unit cell divided into triangles and semi-circles.

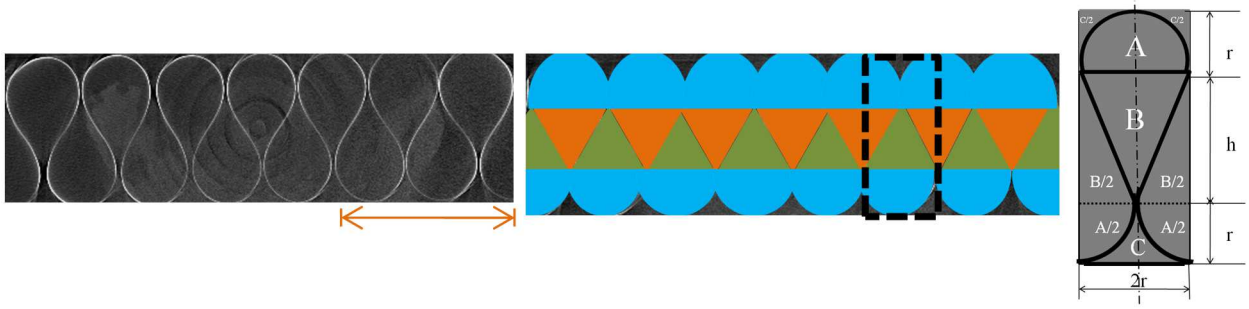

Figure 4 (Left) Axial slice of a "Teardrop" cell from X-ray Computed Tomography (scale-10 mm); (middle) row of teardrop lattice broken into fundamental shapes of triangles and semi-circles; (right) one "teardrop" unit cell.

Relative density is the ratio of cell wall area to solid area in a unit cell.

$$\frac{\rho^*}{\rho_S} = \frac{(Perimeter of\ A + Perimeter of\ B + Perimeter of\ C) * t}{(Area\ of\ A + Area\ of\ B + Area\ of\ C)}$$

For a "teardrop" unit cell, "*r*" is cell size (cell size in a hexagonal cell is denoted by "*l*") and "*t*" is cell wall thickness, "*a"* is edge length of triangle given by $\sqrt{h^2 + r^2}$; by approximating *h*~3*r* (based on measurements of first samples), the relative density for a "teardrop" unit cell can be written as

$$\frac{\rho^*}{\rho_s} = \frac{\pi r t + 2at + \pi r t}{\pi r^2 + 6r^2 + 2r^2} \tag{2}$$

$$\frac{\rho^*}{\rho_S} = 1.13\left(\frac{t}{r}\right) \tag{3}$$

2.3.2 Compressive Strength (σ_{el}^*)

Strength capabilities of cellular solids are governed by semi-empirical relationships of type

$$\frac{\sigma^*}{X_S} = C\left(\frac{\rho^*}{\rho_S}\right)^n \tag{4}$$

where X_s is the property of solid cell wall material, *C* and *n* are constants dependent on cell shape and deformation mechanism. When loaded in the out-of-plane direction, possible failure mechanisms of adhesively bonded honeycombs can be

(1) Elastic/Plastic buckling of cell walls leading to non-linear behavior.

(2) De-bonding of cell walls.

(3) Fracture.

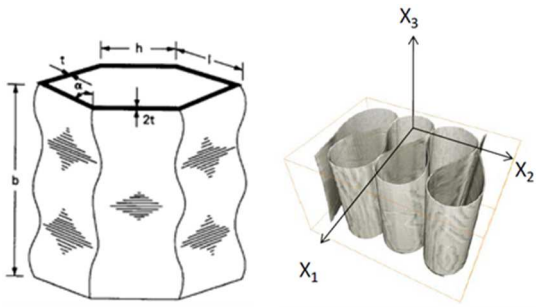

Figure 5 (left) Hexagonal cell showing cell wall buckling [54]; (Right) Reconstructed Computed Tomography 3-D perspective of "teardrop" cells.

A re-constructed CT image of teardrop cells showing the in-plane *(X_1 and X_2)* and out-of-plane *(X_3)* directions is shown in Figure 5. In the out-of-plane *(X_3)* direction, post buckling stress is considered the "failure stress" of honeycomb, since separation of the walls at adhesive joints is seemingly inevitable when deformation of the honeycomb is large [36].

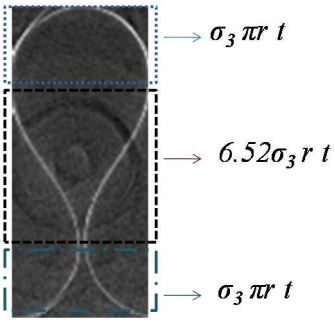

Figure 6 Load carried by each section of unit cell.

Load carried by each divided area of a teardrop unit cell is shown in Figure 6. For uniform compression of cell walls, each wall is considered to carry an equal amount of compressive stress, σ_3, while the global stress is denoted σ^*_3.

Load carried by the unit cell is given by $10\sigma_3^* r^2$

Equating force equilibrium one gets

$$\sigma_3^*(10r^2) = \sigma_3(\pi rt + 6.52rt + \pi rt)$$

This implies that compressive stress in the cell wall is inversely proportional to the relative

$$\frac{\sigma_3^*}{\sigma_3} = 1.28\left(\frac{t}{r}\right) \tag{5}$$

density of honeycomb. Based on earlier assumptions, elastic buckling stress (σ_{cr}) can be evaluated using Euler's buckling formula for a plate per unit width [55] given by

$$\sigma_{Cr} = \frac{\pi^2 K E_S}{12\left(1-\upsilon_S^2\right)}\left(\frac{t}{b}\right)^2 \tag{6}$$

Where υ_S is Poisson's ratio of solid material, K is the buckling coefficient, t is the wall thickness and b is the unloaded edge length.

K is a function of cell edge conditions and the ratio of length of lateral edge (unloaded) and b, the loaded edge length [56].

Now substituting the value of σ_{cr} in σ_3 we get

$$\sigma_3^* = \frac{K\pi^2 E_S}{12(1-\upsilon_s^2)}.\left(\frac{t}{r}\right)^2 * 1.28\left(\frac{t}{r}\right)$$

From which, the analytical model for axial compression strength of AMH is given by:

$$\left(\frac{\sigma_3^*}{E_S}\right) = 0.1\frac{K\pi^2}{(1-\upsilon^2)}\left(\frac{t}{r}\right)^3 \tag{7}$$

where σ^*_3 is the axial compression strength of honeycomb in the out-of-plane (X_3) direction. r is the teardrop cell size of honeycomb.

"K ", the buckling coefficient is determined by edge conditions of neighboring cell walls. Buckling of each cell wall in a honeycomb is considered similar to buckling of straight columns based on Euler's formula. The value of "*K"* is estimated by assuming cell edge conditions. Each individual cell wall is restricted by neighboring cell walls on their edges

and stabilizing face sheets (for a sandwich panel, and in compression between platens) on the top and bottom. If all edges are assumed clamped, then one gets the upper bound of compressive stress. If all edges are assumed simply supported, then one gets the lower bound of compressive stress. In reality, the strength of neighboring cell walls are stronger than that provided by simply supported edges. "*K*" is assumed to lie between these two extreme conditions for adhesively bonded honeycombs [36]. The buckling co-efficient (*K*) for the various end conditions is presented in Figure 7.

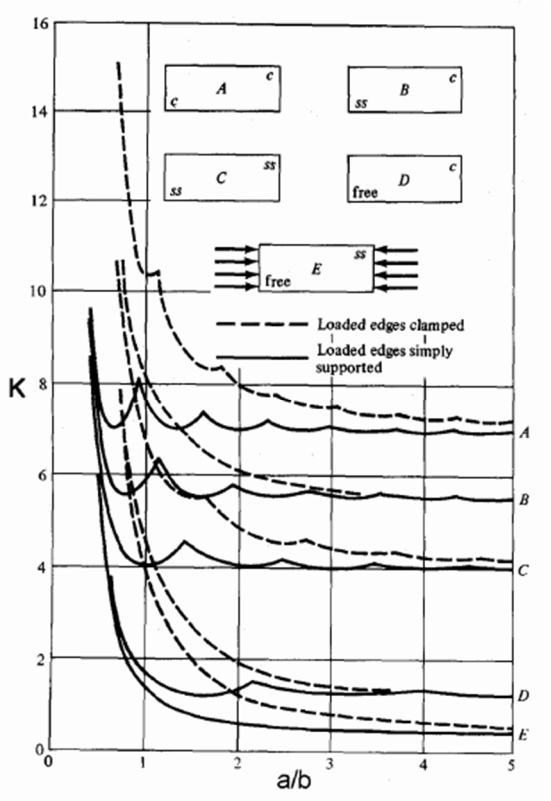

Figure 7 Buckling Co-efficient for different boundary conditions [56].

For Aluminum honeycombs, an upper bound of K=5.73 has been proposed based on formulae from Roark and Young. Also, K=3.29 has been termed a "realistic value" in Ashby's paper on out-of-plane properties of honeycombs, assuming simply supported

edges on all cell edges [36]. This is applicable for honeycomb heights that are at least 3 times the cell size ($h > 3l$). Based on the results from experimental testing of AMH, K=2.5 was obtained. Experimental results described in Table 1 show this. Respective optimum design densities for AMH (using amorphous $Fe_{45}Ni_{45}Mo_7B_3$ alloy) to exceed Aluminum honeycombs are presented in Figure 8.

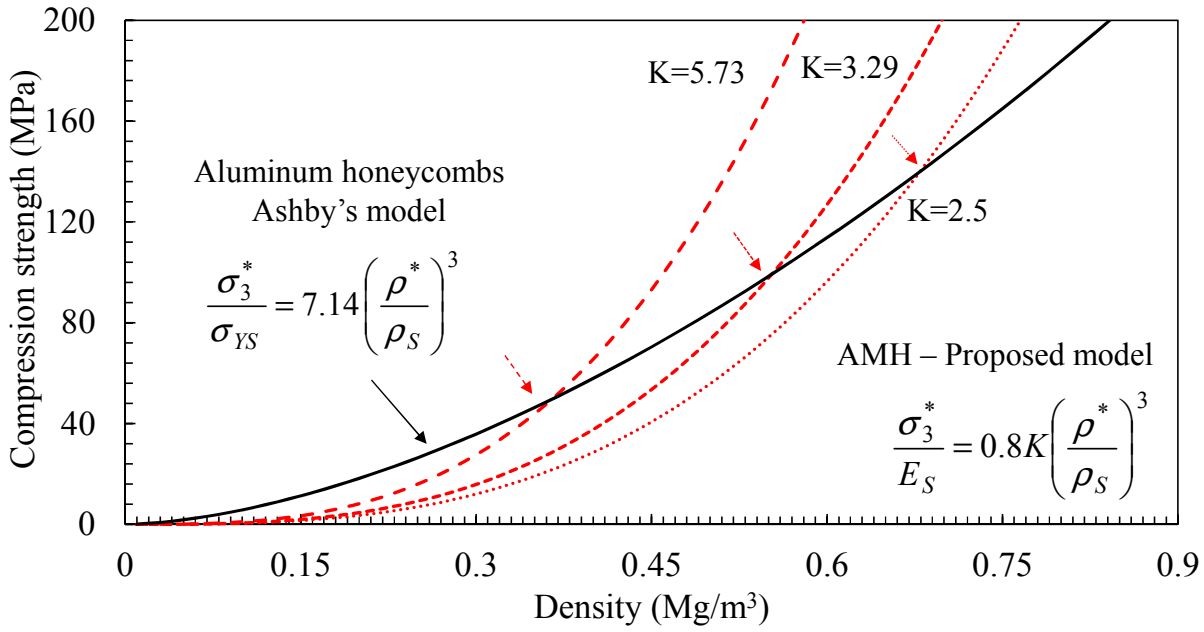

Figure 8 The optimum density of AMH to exceed compressive strength of Aluminum honeycombs based on Ashby's model for three different buckling coefficients in the proposed model. The three dotted arrows show points where minimum densities for different "K" values would exceed the strength of Aluminum honeycombs.

2.4 Processing Methods in Amorphous Metal Honeycombs

In earlier work [29, 33], amorphous $Fe_{45}Ni_{45}Mo_7B_3$ honeycombs were manufactured using a *Winding method* by folding the ribbon onto itself, using the high elastic strain of $Fe_{45}Ni_{45}Mo_7B_3$ ribbons. Cells were fixed using adhesive. First samples had a cell size of 3 mm, a 29 μm cell wall thickness, and 97% porosity. Another method (*pin method)* was also devised to improve the uniformity of cells and space [57].

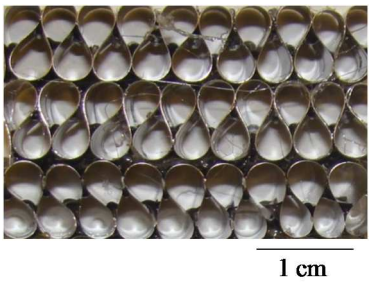

Figure 9 Amorphous $Fe_{45}Ni_{45}Mo_7B_3$ sample with "teardrop" unit cells.

Both, the *winding method* (Appendix-I) and the improved version [58], had limitations on achieving smaller cell sizes. They induced cell wall misalignments and bonding mismatch with cell irregularity (Figure 9). Similar imperfections have shown to reduce strength and modulus of a honeycomb by up to 40% [29, 32]. The proposed model predicts an AMH 1.1 mm cell size to exceed the theoretical specific strength of Aluminum honeycombs. A *comb method* (Appendix-II), capable of manufacturing this cell size, was developed[3]. The high elastic limit of amorphous $Fe_{45}Ni_{45}Mo_7B_3$ ribbon allows weaving it around a range of curvatures. The Comb method involved a pin fixture to form cells. A fixture built to attach and remove pins of 1.1 mm diameter was developed, to weave the ribbon in a sinusoidal fashion. A notched clamping fixture with cut sections matching the lateral external profile of an AMH row was used to secure each row. Alignment and cell size are controlled through these steps. Pins are then pushed out of the fixture and stabilizing combs inserted along the central longitudinal plane. This secures individual cell joints in the row. Individual rows are then stacked and bonded using an adhesive to form AMH. A step-wise procedure is presented in Appendix II Manufacturing AMH with a cell size of 1.2 mm using the Weave and Comb method.

[3] In collaboration with MetCel LLC., Tulsa, OK and Concurrent Design Inc., Austin, TX.

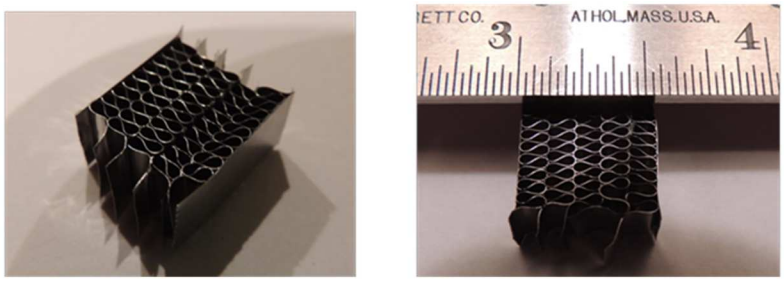

Figure 10 AMH prototype of Cell size 1.1 mm; first prototype with 4 rows

Other methods such as bonding ribbon reinforcements on the teardrop row were also tested to make AMH with tailored cell sizes with minimized defects. Based on strength, density, and ease of application; different adhesives were tested for use in inter-cellular and inter-row bonding of AMH.

Figure 11 Nanosteel honeycomb with "teardrop" cells with 1.2 mm cell size.

A higher modulus Nanosteel alloy with "teardrop" cells of size 1.2 mm is also shown in Figure 11. Using Nanosteel ribbons of width 5.73 mm and 35µm thickness different densities were manufactured by using reinforcements and tested for their axial mechanical properties.

2.5 Experimental testing and Validation

Compression testing in the out-of-plane direction was performed using a hydraulic-driven Instron universal testing machine. Sample sizes and compression rates were chosen based

on American Society for Testing and Materials, ASTM [4] methods. For comparison, Stainless steel 304 honeycombs, with teardrop cells using a similar manufacturing method and hexagonal aluminum honeycombs with a closely matching density were tested.

Figure 12 shows stress-strain curves. The difference in compressive strength of AMH and Aluminum 5052 honeycomb is denoted by $\Delta\sigma$.

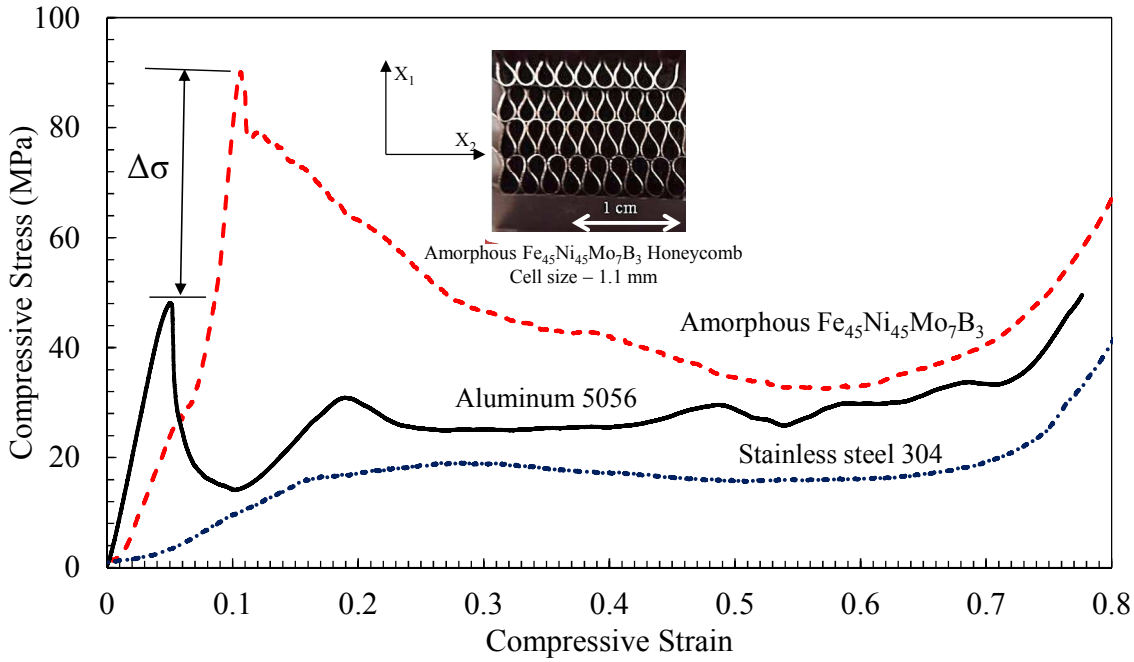

Honeycomb material	Cell shape	Density (Mg/m^3)	Specific Strength (KNm/Kg)
Amorphous $Fe_{45}Ni_{45}Mo_7B_3$	Teardrop	0.6	150
Aluminum 5056	Hexagon	0.4	122
Stainless Steel 304	Teardrop	0.7	27

Figure 12 AMH with a 1.1 mm cell size under out-of-plane compression

[4] ASTM C365/C365M-11a "Standard Test Method for Flat-wise Compressive Properties of Sandwich Cores"

AMH, in a density range of 0.3 Mg/m^3 to 0.6 Mg/m^3 were manufactured using different adhesives and forming methods, then tested for compression behavior. Experimental results are plotted with the proposed analytical model, compared with Ashby's plastic yielding model for aluminum honeycombs, and published data from industry data sheets [26] in Figure 13.

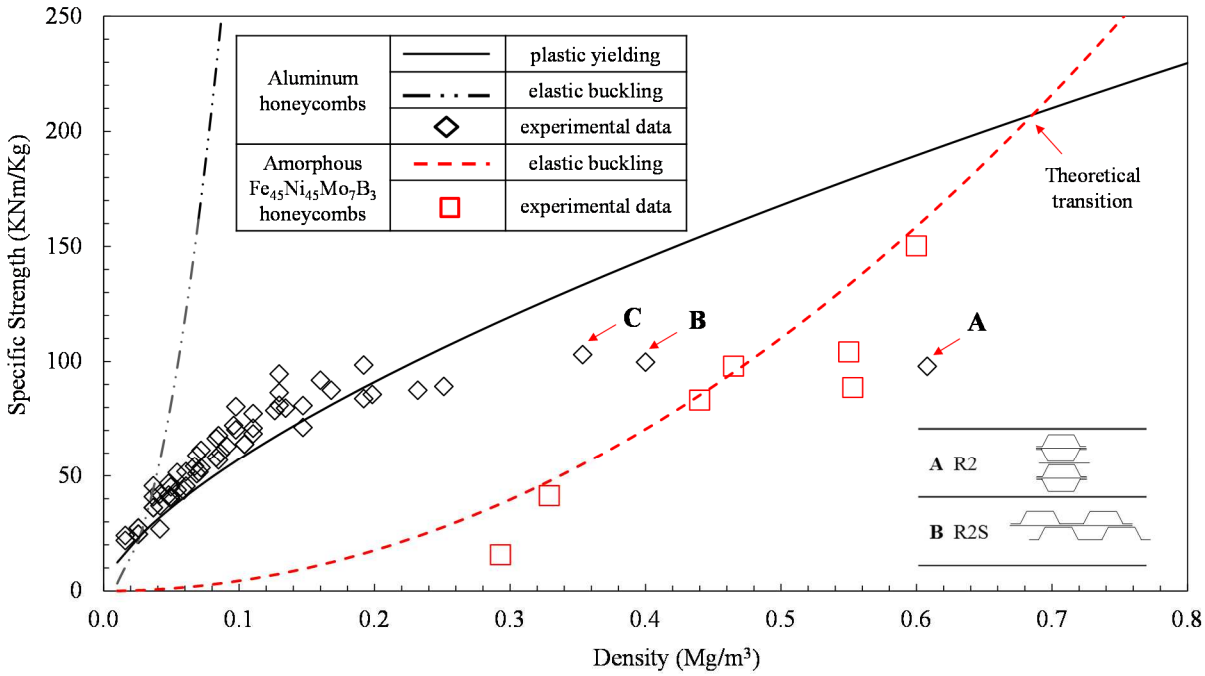

Figure 13 Specific Strength chart showing the highest specific strength honeycombs plotted with theoretical predictions. Lines represent theoretical predictions and symbols are experimental data. Note: Insets "A" refers to a reinforced hexagonal cell (R2), "B" refers to staggered reinforced hexagonal cell (R2S), and "C" refers to standard hexagonal cell from industry datasheets.

2.6 Discussion

It is evident from Figure 13, that the specific strength of Aluminum honeycombs (specific strength is density normalized axial compression strength), follows Ashby's plastic yielding model and not an elastic buckling model.

For in-plane compression (X_1 and X_2), this has been explained as a function of a critical *t/l* ratio where *t* is honeycomb wall thickness, *l* is to cell size. The critical *t/l* ratio at which elastic buckling precedes plastic yielding is a function of σ_{ys}/E shown by Ashby [23] as

$$\left(\frac{t}{l}\right)_{crit} = 3\frac{\sigma_{YS}}{E_S}$$

The σ_{ys}/E value for many crystalline metals is on the order of 10^{-3}. For example, elastic buckling can occur in aluminum honeycombs for densities lower than 0.04 Mg/m^3. So low, that it prevents elastic buckling in practical honeycomb structures. (σ_{ys}/E is 0.005 for Al 5056). However amorphous metals have a relatively higher σ_{ys}/E ratio, by an order of magnitude, allowing elastic buckling to be easily achievable in practical densities. Recent work [27] on the characterization of BMG honeycombs has shown the influence of *t/l* on resulting strength in the in-plane directions for demonstrated densities of 0.9 – 3.4 Mg/m^3. Honeycombs are strongest in the out-of-plane direction, as compared to the in-plane directions. With amorphous metals having greater σ_{ys} than E_s compared to crystalline alloys of Aluminum and Steel, taking advantage of their high yield strength is optimum.

In the out-of-plane direction (X_3), assume each honeycomb cell wall to be a column with boundary conditions defined by neighboring cell walls. The ratio of wall thickness and honeycomb (*t/h)* defines the deformation mechanism. That is, whether the cell wall behaves like a long, intermediate, or a short column. Long columns fail structurally with buckling failure, while short columns fail materially with yielding failure.

Respective critical failure loads are

Long column $$\frac{\pi^2 E_S I}{L^2} \quad (8)$$

Short column $$\sigma_{cr} A \quad (9)$$

Where E_S is Young's modulus of solid material, I is moment of inertia, L is length of the column, σ_{cr} is critical stress, and A cross-sectional area.

The moment of inertia I, of a honeycomb cell wall is given by $lt^3/12$, L denotes h which is honeycomb height, and A is given by lt. Substituting these values and equating the critical stress shown in equations (4) and (5) gives

$$\left(\frac{t}{h}\right)_{crit} \leq 1.09\sqrt{\frac{\sigma_{cr}}{E_s}} \quad (10)$$

Equation (10) shows the critical ratio of honeycomb cell wall thickness to honeycomb height, beyond which elastic buckling precedes plastic yielding. For amorphous $Fe_{45}Ni_{45}Mo_7B_3$, with a thickness of 0.029 mm, plastic yielding can happen at a honeycomb height of 0.2 mm. For other materials, validity of equation (10) depends on the abovementioned postulations, intrinsic material behavior (elastic or elastic-plastic), and proportionality limits.

Using the proposed analytical model equation (7), optimum theoretical densities of AMH were predicted for different K values. A cell size of 1.1 mm was targeted. AMH samples were produced with 6 different densities and tested for their compressive

mechanical response to validate the model. Their densities, type of adhesive used and measured compressive strength are shown in Table 1.

Table 1 Measured compressive strength of AMH

Adhesive	ρ^*/ρ_s	Density (Mg/m^3)	Compressive Strength (Mpa)	Specific Strength (KNm/Kg)	Mfg. method (Section 2.4)
Hot melt	0.037	0.29	4.60	15.70	Winding
DP 110	0.042	0.33	13.60	41.34	Pin
DP 420	0.070	0.55	49.03	88.67	Pin
DP 420	0.056	0.44	36.60	83.18	Pin
Nolax	0.070	0.55	57.30	104.18	Comb
Nolax	0.059	0.47	45.55	97.96	Comb
3M 3109	0.076	0.60	90.11	150.18	Comb

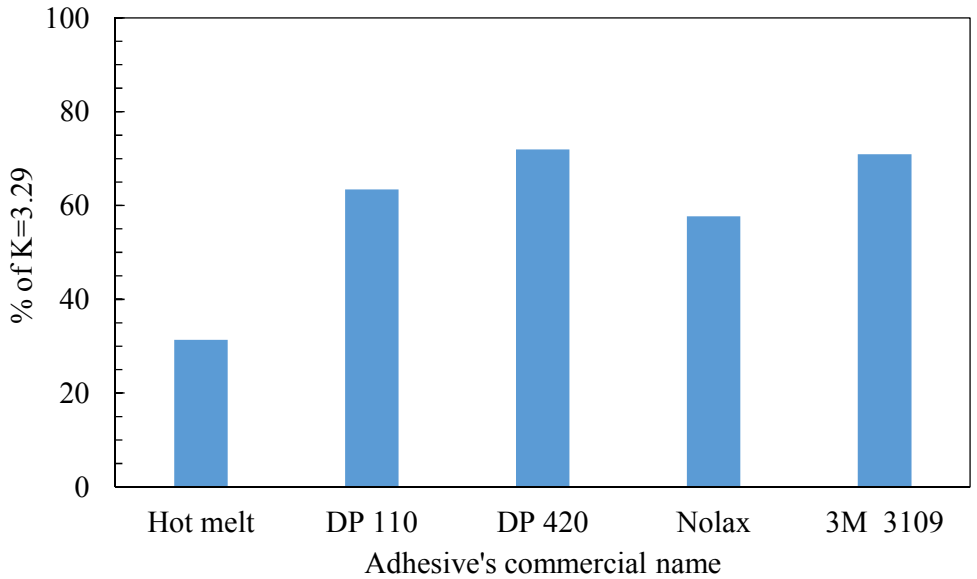

Figure 14 Buckling coefficient estimated from proposed model. Y-axis is plotted as a function of Ashby's proposed "*K*" value (*K*=3.29) for adhesively bonded honeycombs.

The buckling coefficient (*K*) was estimated for each adhesive listed in Table 1 from the proposed model. "K" as a function of adhesive is plotted in Figure 14. The type of adhesive had an influence on measured density, and resulting compressive strength. Modified epoxy from 3M (trade name: 3M 3109), gave the best compressive strength.

Defects had an influence on the quality of AMH and measured experimental values. AMH samples had occasional cell wall misalignments in the range of 10^{o} and bonding mismatches (example shown in Figure 9). This induces an artificial affine shear component in deformation during axial compression. Therefore, not all honeycomb rows were loaded perpendicular to the cell axis. Adhesive bond strength between rows were limited, which lead to de-bonding as load was applied (Figure 15).

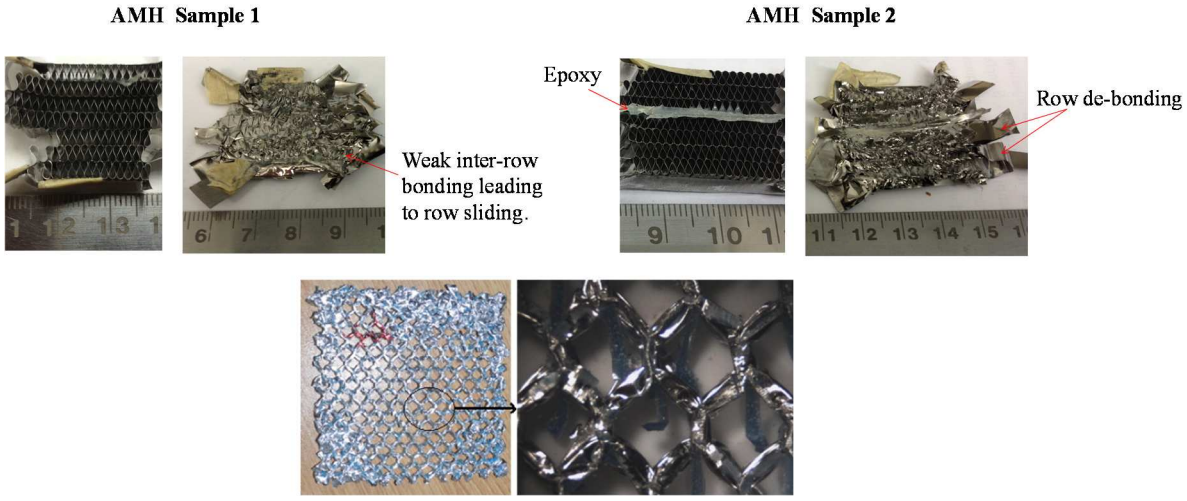

Figure 15 Pictures of AMH teardrop samples of cell size 1.1 mm before and after axial compression (top), Hexagonal Aluminum honeycombs after compression; note the retained shape of the hexagon after compression, showing strong inter-cellular bonding [3].

Measured densities of AMH samples and compression results indicate the influence of adhesives on honeycomb behavior. This suggests a need for stronger inter-cellular bonding between the cells. The buckling co-efficient "*K*" is a function of cell edge conditions, inter-cellular bonding strengths and inter-row bonding between neighboring rows. Double-walled hexagons have better inter-cellular bonding compared to these teardrop cellular structures. As would be expected, hexagons have a more closely packed structure with a higher relative density.

The proposed model and experimental AMH results are plotted in Figure 16, along with the highest specific strength aluminum honeycombs, BMG honeycombs, ceramic nano lattices, and a few conventional high specific strength materials for reference.

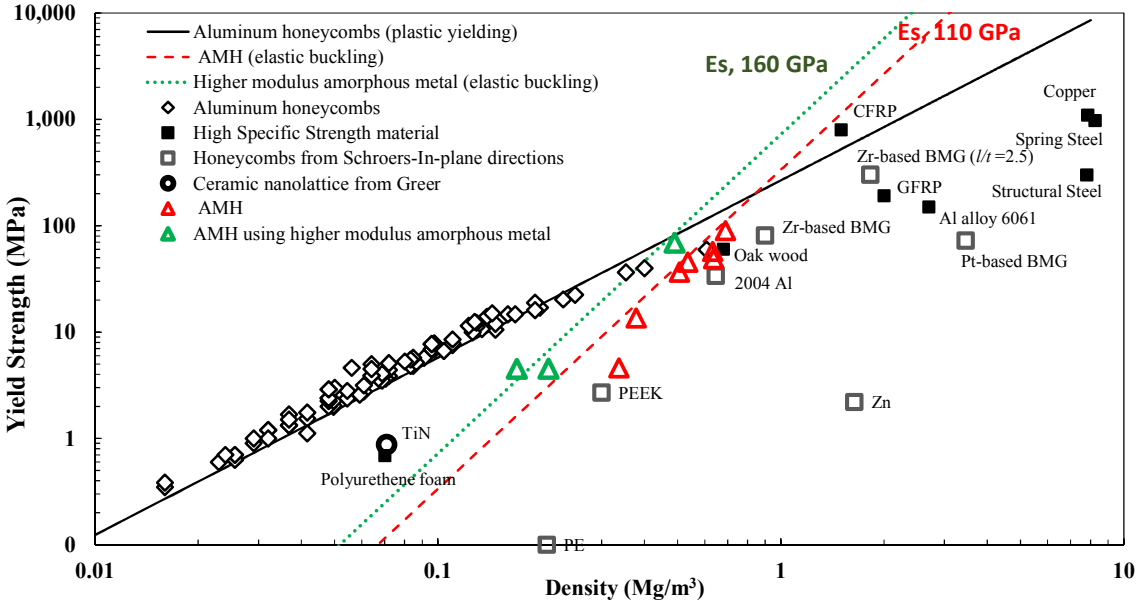

Figure 16 Yield Strength of AMH and Nanosteel honeycombs compared to other high specific strength materials. Lines represent theoretical predictions and symbols are experimental data.

This result further validates the analytical model. Data for compressive strength of hexagonal aluminum honeycombs follows Ashby's plastic yielding model and not an elastic buckling model, up to a maximum of 60 MPa. Until now, this was the highest specific strength honeycomb. With high σ_y/E values, and a l/t ratio greater than a critical value, elastic buckling is possible in compression of amorphous honeycomb walls. New honeycombs made using Amorphous $Fe_{45}Ni_{45}Mo_7B_3$ and Nanosteel ribbons that for the first time exceeds this limit are shown in this work. This shows new high specific strengths are possible for thin walled metallic honeycombs using amorphous metals.

A theoretical transition between a maximum specific strength with aluminum honeycombs to a higher maximum for amorphous metal honeycombs is also suggested by the models.

This transition has occurred before reaching the predicted density. This has to do with several factors including inter-cellular bonding strength and adhesive mass. Wall thicknesses, base material plasticity, and plastic hinges limit the theoretical strength of aluminum honeycombs. Processing methods restrict achievable densities. For higher densities, some options include modifying the cell structure with the use of cell dividing sheets, called reinforcements, as indicated by data point "A" in Figure 13. But this does not typically provide as much benefit for out-of-plane compression as the more difficult option of simply reducing the hexagonal cell size. Reducing adhesive mass and improving inter-cellular bonding strengths are important to achieve the potential of honeycombs, including AMH.

2.7 Chapter Summary

A new analytical model was proposed to predict relative density and axial compressive strength of honeycombs with a "teardrop" cell shape. An optimum theoretical density at which axial compression strengths of Amorphous $Fe_{45}Ni_{45}Mo_7B_3$ honeycombs exceed theoretical strengths of aluminum honeycombs was predicted. AMHs using two different alloys were manufactured using a new approach. AMH densities of 0.3 Mg/m^3 to 0.6 Mg/m^3 were demonstrated. Results from experimental testing of axial compression strengths of AMH validated the proposed analytical model. AMH with a density of 0.6 Mg/m^3 with a cell size of 1.1 mm showed a higher axial compressive strength compared to aluminum honeycombs published in literature. The proposed model also shows that a higher maximum yield stress is achievable by improving inter-cellular bonding. Higher σ_{ys}/E_s alloys allow manufacture of honeycombs that can elastically buckle in a realistic t/l ratio. Other amorphous alloys, with higher Young's moduli are beneficial as they could

enable honeycombs with higher axial compressive properties. Defects and imperfections in AMH samples, affected the resulting maximum strengths. The buckling coefficient plays a crucial role in achievable honeycomb strengths. Improving the buckling coefficient by improving inter-cellular bonding and reduction of nonfunctional structural mass such as excess adhesives, helps improve specific strengths. This provides the motivation for Chapter 3.

CHAPTER III

INTER-CELLULAR BONDING IN AMORPHOUS METAL HONEYCOMBS

3.1. Introduction

Inter-cellular bonding affects the axial compressive strength of AMH. With limited bonding area and lack of plastic deformation, a significant force is required to create a "teardrop" cell. A force is also required to hold the individual rows together to form the honeycomb network. These forces can also be looked at in terms of residual stresses.

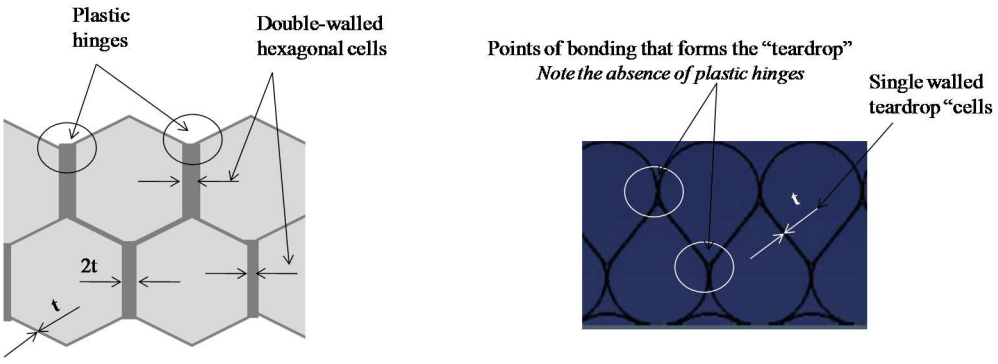

Figure 17 Differentiation of two cellular geometries. Note the difference in bonding areas and absence of plastic hinges in the teardrop structure.

Residual stresses at the nodes, (teardrop cell) shown in Figure 17, can potentially maintain the cell position, meaning little to no bonding is required. Adhesives or welding could provide the force necessary to hold the cell shape. Stresses at the inter-row nodes are not only compressive, but also acts as a shear force tending to open the teardrop cell. These stresses are important in maintaining the cell shape and cell closing force.

The force required to maintain a teardrop cell is a function of adhesive, bonding area, cell size, and material plasticity. Teardrop cell shapes for honeycombs, discussed in the previous section, are formed by folding the ribbon on to itself. High stresses (2 GPa) and elastic limits (2%) in amorphous ribbons, require significant bonding force to form a teardrop cell.

In a teardrop shape, the high elastic limit of amorphous ribbons allows for storing energy in the form of residual stress and remains elastic up to a stress limit. Beyond this limit, plastic deformation occurs as an onset of shear bands. This is not the case for honeycombs with crystalline base materials. Their order of magnitude lower elastic limit and their extensive tolerance for plastic deformation enable the formation of a hexagonal structure where no force is required to suppress elastic relaxation.

Welding has been used in inter-cellular joining of Aluminum and Steel honeycombs. For materials with grain boundaries, methods like resistance spot welding have been successful allowing re-solidification and grain-growth, both in the bond and heat affected zones. Amorphous metals do not have grain boundaries, and with a limited cooling window (time to crystallization), rapid cooling methods are necessary to weld and maintain an amorphous state. While different welding methods have been demonstrated for BMGs with lower critical cooling rates, successful welding of MGs without crystallization has been a challenge.

3.2 Background on Welding of Metallic Glasses

Amorphous Metal Ribbons (AMR) are produced using slip casting at a critical cooling rate of 10^{-5} to 10^{-6} K/s. A limitation of amorphous alloys is their tendency to crystallize on

heating. Based on this, joining methods for amorphous alloys can be grouped into two categories [59] depending on crystallization temperature.

(1) Bonding methods under conditions lower than their crystallization temperature; typical examples include adhesive bonding, brazing or soldering, cold pressure welding, explosive welding, and ultrasonic welding.
(2) Other methods involving temperatures greater than their crystallization temperature and at short time intervals; examples include resistance welding, electron beam welding, and laser beam welding.

Welding amorphous alloys is a non-equilibrium process of reheating and cooling a disordered microstructure with small solidification shrinkage. Cooling an amorphous alloy is a non-equilibrium process leading to Coring. Coring is the formation of higher melting temperature elements in external layers. It is important to suppress grain growth that causes cracking, while also avoiding deviation from the glass forming composition. The amorphous state of the weld interface needs to be retained for a successful bond. When the interface temperature is less than T_g (Glass Transition temperature), the presence of a surface oxide film often prevents bonding. Subsequently, when temperature is equal to or exceeds T_g, there is a super cooled liquid state; where surface oxides either need to be broken or prevented from oxidation to form successful bonds. Surface contact can be created at an atomic scale through fresh surfaces to form an amorphous weld [60]. Other welding work [61-63] has shown evidence that crystallization during welding deteriorates properties with cracks formed due to surface oxidation.

Research on achieving higher length-scales of BMGs has attracted interest on welding. Pulse-current, Friction [60, 64, 65], and Electron beam welding techniques [66-69] have been reported to work on BMG-BMG and BMG-crystalline material combinations. Other welding studies reveal that Zr based and Pd based bulk glassy alloys can be joined together by the use of Joule heating. Work [63] on Zr-based metallic glass showed that high power laser welding was suitable for joining amorphous Zr-based BMG with no crystallization around the heat affected zone (HAZ). In other studies on amorphous foils, Capacitor discharge welding has been reported to successfully weld Co- and Fe- based amorphous foils with no measurable oxides or crystallization [70]. A Ni-based glassy alloy was reported weldable using electron beam welding with no crystallization [71]. Ultrasonic welding and explosive welding have proven to work on $Fe_{40}Ni_{40}P_{14}B_6$ amorphous foils [72].

Laser welding has been most successful in welding metallic glasses, because of the relatively smaller melting volume of base material involved [73, 74]. Successful welding has been reported for $Ni_{53}Nb_{20}Ti_{10}Zr_8Co_6Cu_3$ metallic glass foil of 25 μm thickness using high power fiber laser welding [75]. The same work also indicates that weld rate affects crystallinity. High quality welds have been demonstrated on $(CoFe)_{70}(MoSiB)_3$ foils using Nd:YAG laser welding, but limited to a narrow window of voltage, pulse duration, and focus position [59]. Fe- and Co-based thin amorphous ribbons were tested for weldability using spot welding [61]. Results from welding $Fe_{40}Ni_{40}Mo_4B_{16}$ showed embrittlement of spot welded regions, and crystallization which caused deterioration in joint strength. Results from this work indicate that spot weld-ability of AMR largely depends on foil

chemistry. These all provide a background of how welding of metallic glasses have been investigated both in ribbon and bulk form.

This chapter investigates inter-cellular bonding strength in amorphous $Fe_{45}Ni_{45}Mo_7B_3$ honeycombs. Two joining methods are evaluated, adhesive bonding and welding. Using experimental testing and analytical models, the required minimum adhesive and weld force to form a teardrop cell as function of cell size is predicted. Success and challenges of both joining methods are compared.

3.3 Materials and Methods

Amorphous $Fe_{45}Ni_{45}Mo_7B_3$ ribbons of 8 mm width and 29 μm thicknesses were selected for this study. Different adhesives were chosen for lap joint shear strength testing (Table 2).

Table 2 Adhesives selected for Lap joint shear testing

Adhesive type	Trade name	Form	Manufacturer
Modified epoxy amine	DP 110	Two part paste	3M
Epoxy amine	DP 420	Two part paste	3M
Polyurethene	Gorilla glue	Two part paste	Gorilla Glue company
Epoxy amine	DP 125	Two part paste	3M
Modified amine	1838-L B/A	Two part paste	3M
Modified epoxy	AF 3109 2U	Film adhesive	3M
Modified epoxy	AF 163 2U	Film adhesive	3M
Cyanoacrylate	A 31	Film adhesive	Nolax adhesives
Hot melt	271	Thermally activated	Adhesive Technologies Inc.
Aerosol	78	Spray on	3M

Adhesives were chosen based on compatibility with production method of AMH, adhesive handling time, curing time, viscosity, cost, and ease of applicability. Samples for lap joint shear strength were prepared using each adhesive.

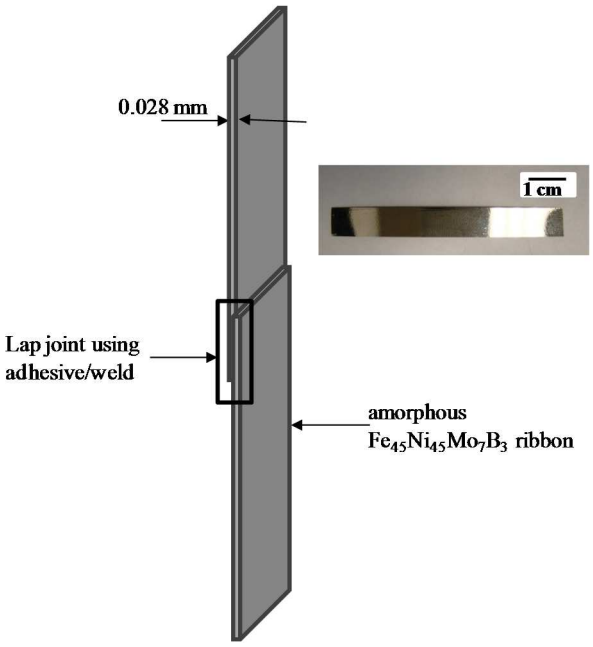

Figure 18 Schematic of a lap joint on ribbon, not drawn to scale: Inset shows a $Fe_{45}Ni_{45}Mo_7B_3$ ribbon.

Two sets of samples, one in the as received condition and the other surface roughened (using 380 grit sandpaper) were prepared. The ASTM[5] was referenced in selecting sample conditions and extension rate. Lap joint bonding areas were measured before testing. Lap joints were allowed to cure and tensile shear strength was measured[6].

The adhesive force required to form a teardrop cell was calculated experimentally by measuring the force required to bend an amorphous ribbon. Amorphous $Fe_{45}Ni_{45}Mo_7B_3$

[5] ASTM D 1002, "Standard Test Method for Apparent Shear Strength of Single Lap-Joint Adhesively Bonded Metal Specimens by Tension Loading (metal-metal)."
[6] Using a 5967 Instron, Universal Testing Machine.

ribbon of known length was subjected to a bending test between compression platens[6]. An extension rate of 0.5 mm/min was used. The force required to close the cell was recorded. The distance between the compression platens was used to calculate cell sizes ($2r$ = "teardrop" cell size in the proposed model).

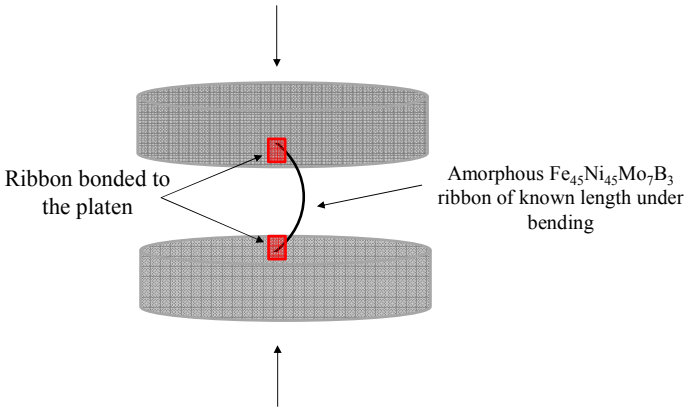

Figure 19 Schematic of the cell closing experiment.

Welding of amorphous $Fe_{45}Ni_{45}Mo_7B_3$ ribbons, was performed under two conditions –

1. Resistance spot welding and laser welding (Table 3)

Table 3 Welding conditions

Type/place of welding	**Miyachi Unitek (Set A)**		**EWI (Set B)**		
Resistance Welding	*Weld Force (N)*	*Hold time (ms)*	*Weld Force (N)*		*Hold time (ms)*
	13.3 – 17.8	150	62		30
Fiber Laser Welding	*Spot size (mm)*	*Power (KW)*	*Type*	*Spot size (mm)*	*Power (KW)*
	0.3	0.2	Pulse	0.006 sec pulse	0.06
			Cont.	0.009	0.06

In laser welding, only the top side of the weld was exposed to an argon atmosphere. Laser welding was done using a 600 W fiber laser at 10% power and a rate of 285 mm/sec.

2. Modified resistance welding using a chilled bath: A modified welding set-up that improves the cooling rate of weld was also developed[7].

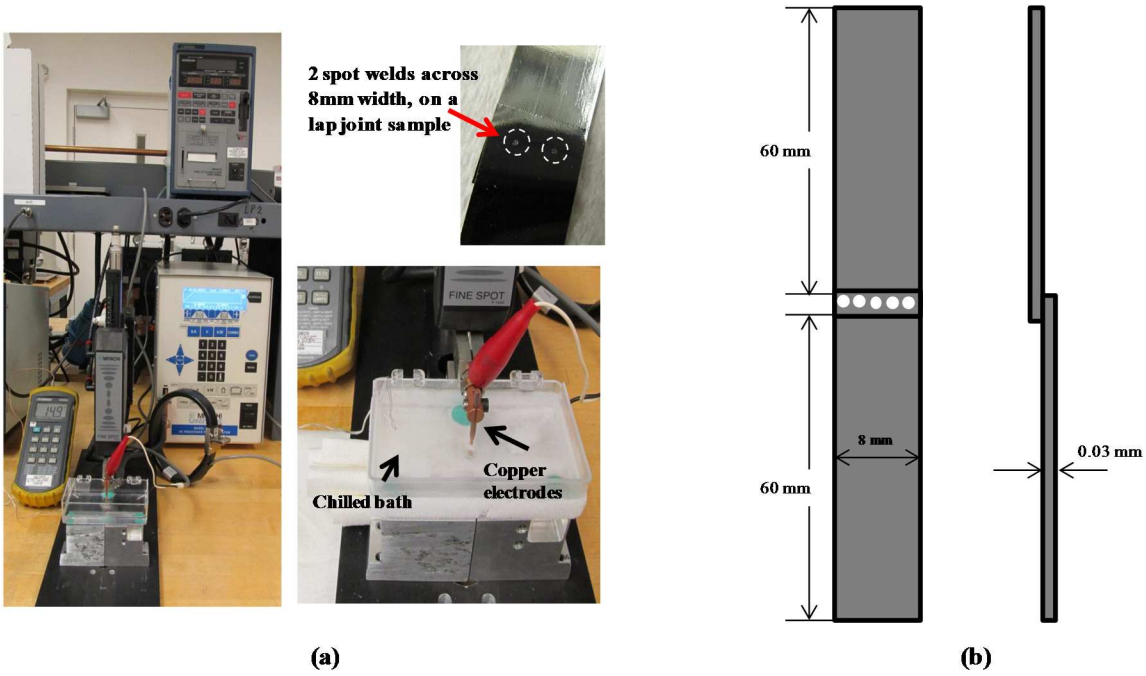

Figure 20 (a) Modified weld-test set-up with a chilled bath and a spot welded lap joint sample with 2 spot welds across the width. (b) Schematic showing front (left) and side (right) view of the lap joint samples; Figure not drawn to scale.

Welding was performed in a chilled liquid bath (containing methanol + dry ice) providing a cooling rate at least twice that of water to prevent crystallization. This is necessary to avoid crystallization induced embrittlement [61]. Weld spots were measured as 400 μm using a laser positioning scale. Temperature in the bath was maintained at -40 to -60 °C. Samples were soaked in chilled bath for 5 seconds prior to welding and submerged in the bath during welding. Three weld forces 22 N (5 lb), 44 N (10 lb), and 66 N (15 lb) were

[7] Welding was performed by MetCel LLC in collaboration with Edison Welding Institute (EWI) in Columbus, Ohio. A Miyachi HF-27 controller, with a Miyachi MH 80-A weld head, using RWMA class 2 copper electrodes was used.

tested. Two spot welds per sample were made on a 8 mm wide sample. 10% of the total current from the weld system was used in these three welding conditions.

Table 4 Welding conditions and parameters

Weld Condition	Force (N)	Time (ms)	Current (kA)
1	22	3	0.6
2	44	6	0.6
3	66	10	0.6

Based on results from mechanical tension testing of lap joints with two spots, welding condition 1 with a force of 22N and a time of 22 ms was chosen for further evaluation. Under this condition, multiple spots were welded across the ribbon width and lap joint samples prepared similarly. Aluminum tabs were bonded on ribbon ends to enable them to grip on Instron fixtures during tension testing.

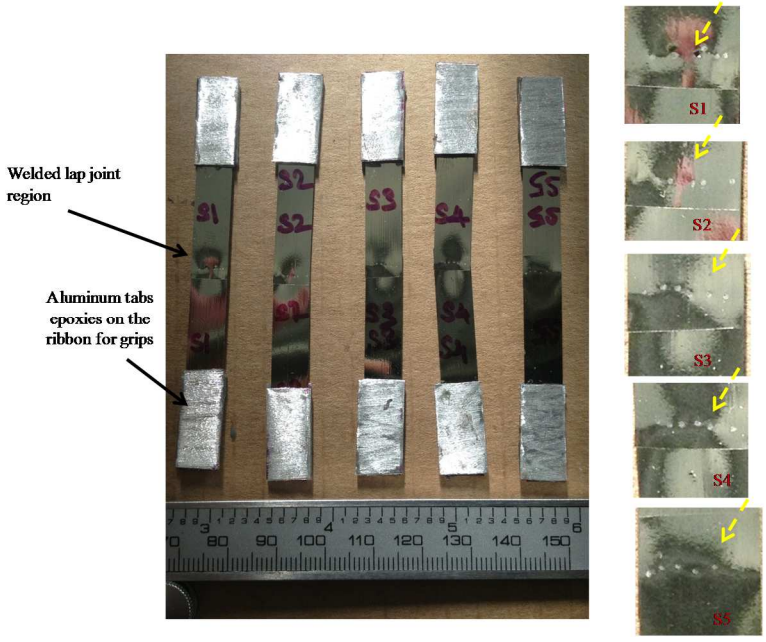

Figure 21 Image of 5 multiple spot-welded samples, prepared for lap joint tests (right), dashed line showing the alignment of weld spots (right).

Table 5 Weld area calculations

Weld area calculations	
Weld spot diameter	400 μm
	0.40 mm
Area of each spot	0.13 mm^2
No. of spots on each sample	6
Total area of weld per sample	0.75 mm^2

Microscopic observations were made before subjecting samples to destructive testing. X-Ray Diffraction, XRD[8] was performed on untreated and welded samples using Cu-K_α radiation at tube parameters of 40kV/40mA. The detector distance to the center of diffraction was kept at 30 cm, which covers approximately an area of 20° in 2θ and 20° in χ with 0.02° resolution. A motorized five axis X, Y, Z (translation), χ (tilt), φ (rotation) stage was used to move the measurement spot to the instrument center within a 12.5 μm position accuracy. Sample positioning was controlled by a video-laser positioning system before each exposure to ensure diffraction patterns came from welded regions of the ribbon.

3.4 Results

The adhesive force recorded during the amorphous $Fe_{45}Ni_{45}Mo_7B_3$ ribbon bending test was plotted with the "teardrop" cell size calculated from platen displacement. Using the

[8] Using a Bruker D8 Discover XRD^2 micro-diffractometer equipped with a General Area Diffraction Detection System (GADDS) and Hi-Star 2D area detector.

resulting ribbon curvature, an inter-cellular bonding force can be estimated from a bending formula given by

$$F = \frac{EI}{Rd} \tag{8}$$

E is Young's modulus of the material, I (moment of inertia, the resistance to bending), R is the radius of curvature, and d is the teardrop cell dimension.

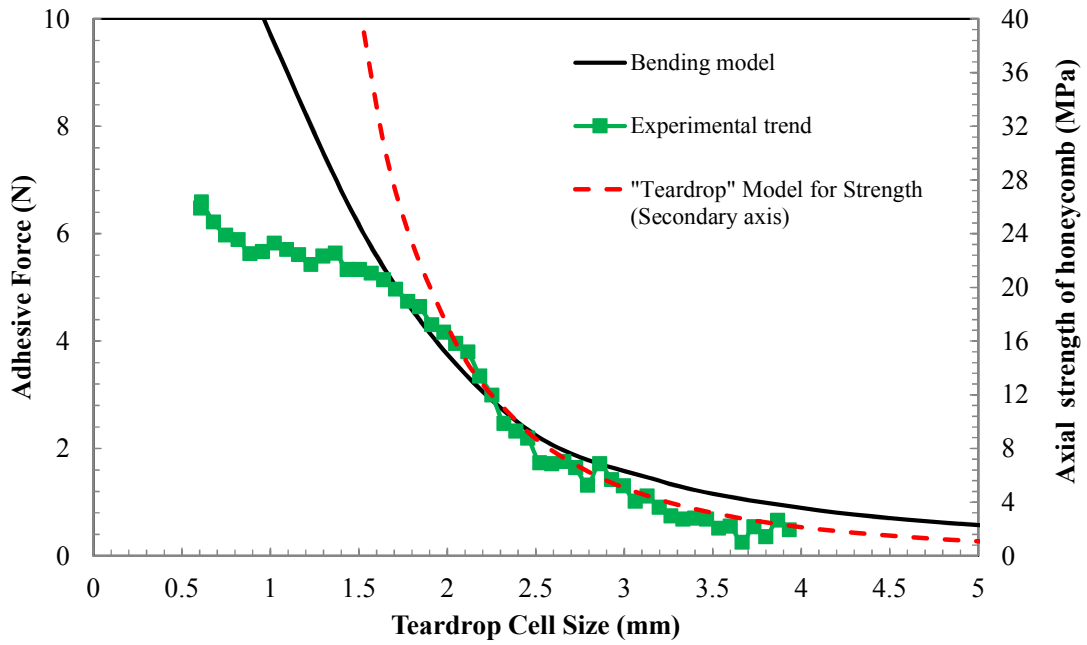

Figure 22 Adhesive force required to from a teardrop cellular structure using an amorphous $Fe_{45}Ni_{45}Mo_7B_3$ ribbon of width 8 mm and thickness 0.029 mm.

Axial strength calculated using the proposed model (Equation 10) is plotted along the secondary y-axis in Figure 22. Tensile shear strength of each adhesive was calculated by normalizing their failure loads with respective bonding areas. The required minimum bonding area to form a 1.2 mm cell size was calculated and shown in Figure 23.

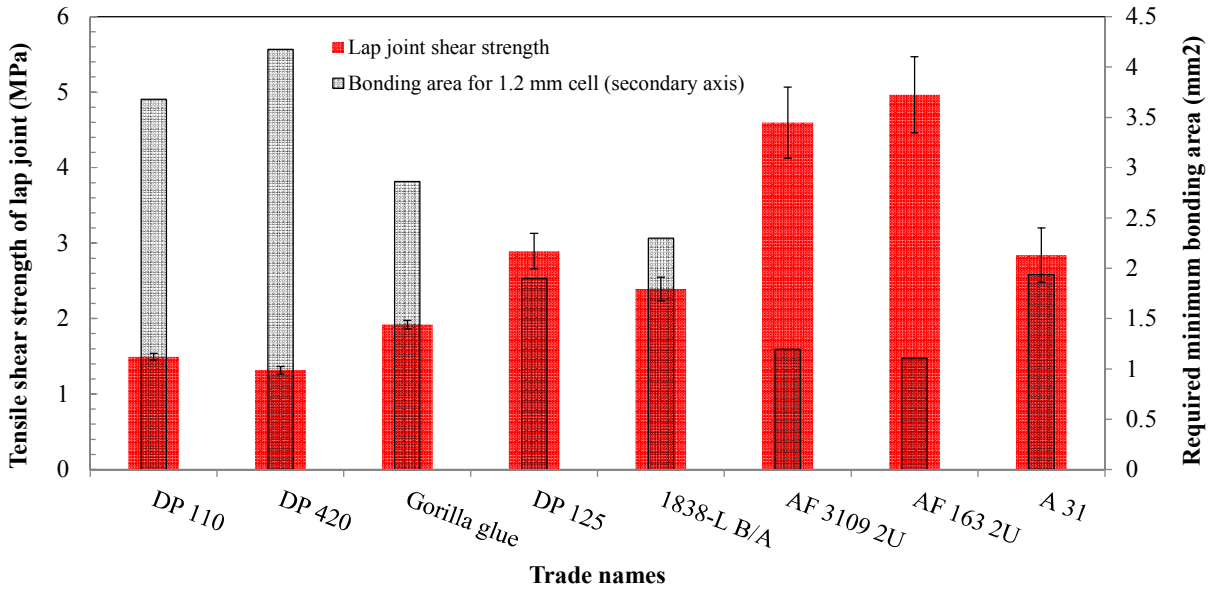

Figure 23 Results from lap-joint shear strength of adhesives on amorphous $Fe_{45}Ni_{45}Mo_7B_3$ ribbons. The secondary y-axis shows the minimum bonding area required for a teardrop cell size of 1.2 mm. Error bars from standard experimental error.

From mechanical tension testing, the modified spot welded samples show a 15X improvement in lap joint strength compared to adhesive bonding. Results from condition 1 (Table 4) showed slightly higher lap joint strength values compared to conditions 2 and 3. Due to force and the weld time involved, condition 1 was chosen. XRD results show no sign of crystallization around the welded spots. Use of a chilled bath helped improve the cooling rate to prevent crystallization. The effect of multiple spot welds on mechanical strength and crystallization of the lap joint were also studied. 6 spot welds were made on 8 mm wide ribbons, and a similar testing procedure was followed to measure lap joint shear strength.

Table 6 Samples S1- had a broken weld nugget on one of the 6 spot welds; Sample S4 had lap joint misalignment on the tension axis.

Sample	Strength (MPa)
S1	8.21
S2	31.26
S3	31.43
S4	23.93
S5	40.35
Average	**27.04**

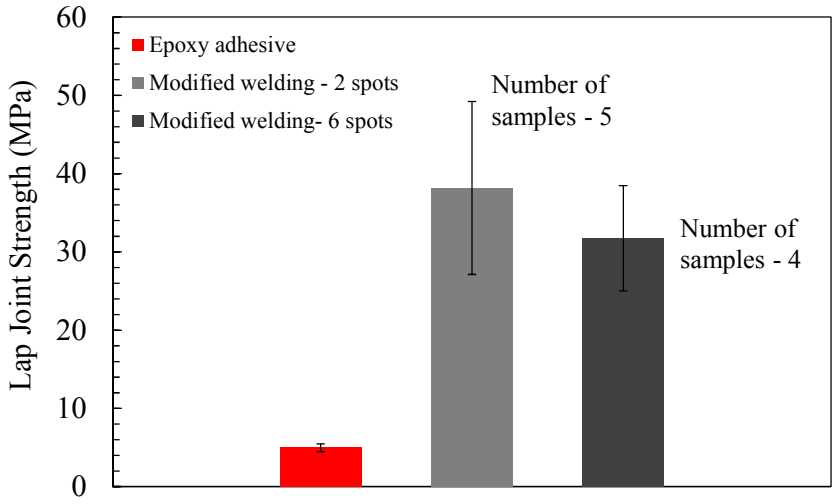

Figure 24 Comparison of lap joint strength from adhesive bonding and welding. Error bars from standard deviation. for modified welding and standard experimental error for adhesives.

3.5 Discussion

Comparing experimental ribbon compression results and the bending model (Figure 22), at a cell size of about 2 mm, there is a deviation from elastic behavior. This indicates the initiation of shear bands. Shear bands, provide additional force required to hold smaller cell sizes, which can be seen from the reduction in slope beyond the 2 mm cell size (Figure 22). Shear bands were apparent in AMH at smaller cell sizes. Their effects on ribbon mechanical properties are briefly discussed in the next chapter.

In comparing different adhesive types, epoxies had better adhesion to the amorphous $Fe_{45}Ni_{45}Mo_7B_3$ substrate. Aerosol based spray had the least strength. The influence of surface treatment (roughing using a sand paper) was not clearly observed. Amorphous ribbons manufactured using the slip casting exhibit different surface characteristics on the two surfaces. Their manufacturing involves a high cooling rate of 10^6 K/s. The ribbon's reflective, smoother side is the surface in contact with the copper disc, while the other side has a darker matte finish. Earlier work on the measurement of surface roughness indicates that the mean roughness is higher for matte side than for reflective side [59]. Bonding surfaces were noted for each of the tested samples, but there was no clear trend for influence of surface roughness on resulting lap joint strength. These results reveal adhesion properties on a comparative scale. Handling time, cost and adhesive viscosity could help in selection of the most suitable adhesive. This is a challenge at smaller cell sizes, due to the significant adhesive force required to hold the cell in shape. Manufacturing limitations for smaller cell sizes can also be overcome by using ribbon reinforcements between cellular rows of the honeycomb. A reinforced design is already used in industry for a crystalline base materials such as aluminum [30].

1. Resistance spot welding and laser welding - Crystallization was observed in ribbon samples using resistance and laser welding, seen from XRD results. In addition to a slower cooling rate (in resistance welding), surface melting and re-solidification govern crystallization. Nuggets of weld spots fractured off the welded sample while handling. XRD measurements on the weld nugget and Heat Affected (HAZ) on the ribbon matched, substantiating deterioration in joint strength due to crystallization. A high cooling rate is preferred to maintain an amorphous weld, and avoid crystallization. With laser welding

techniques, a cooling rate of 10^5 Ks^{-1} is common during re-solidification of melted metals, which is close to the rapid cooling rate of the weld to accommodate solidification shrinkage, without crystallization. However, crystallization of many materials under laser melting has been reported [71, 76-78].

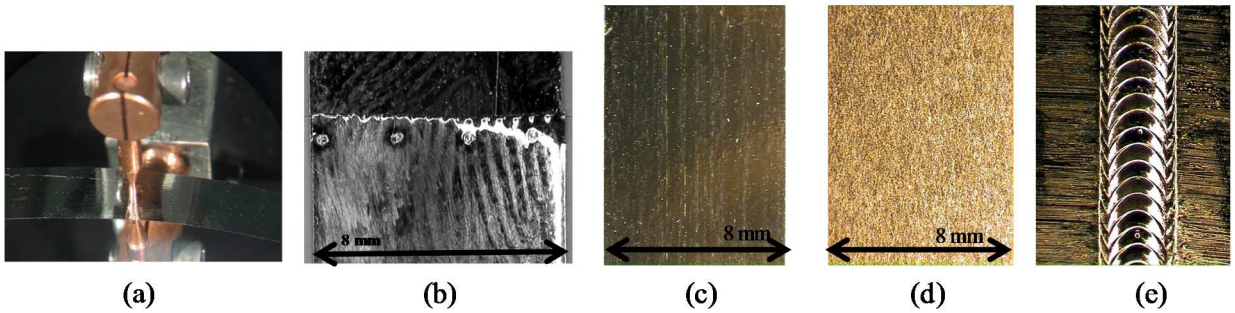

Figure 25 (a) Resistance spot welding of amorphous ribbons between copper electrodes, (b) Welded spots (4) across the 8mm ribbon width, (c) Matte side of the amorphous $Fe_{45}Ni_{45}Mo_7B_3$ ribbon, (d) Matte side of the amorphous $Fe_{45}Ni_{45}Mo_7B_3$ ribbon, (e) Top side of the laser weld.

Amorphous structures do not coherently diffract X-rays, while ordered atomic planes of even small crystal grains cause diffraction. This is easily detected by a 2D detector as a ring. Larger grains show spots.

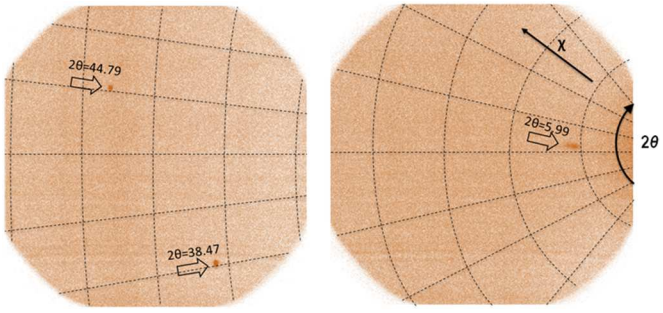

Figure 26 XRD spots as evidence of crystallization from the 13.3 N/150 ms resistance welded specimen.

Figure 26 shows diffraction frames from a resistance welded (13.3 N/150 ms) sample showing isolated spots reflected from single crystal grains. The number of observed spots

depend on beam size, detector area, and the number of crystal grains in the irradiation volume. In practice, only a few grains in an irradiated volume may orient properly to satisfy Bragg's law and diffract. Observations of these spots reveal crystallization of amorphous material at and around the weld due to heat and consequent cooling at an insufficient rate. These spots are observed only in the Heat Affected Zone (HAZ) around welded spots and not elsewhere on the ribbon.

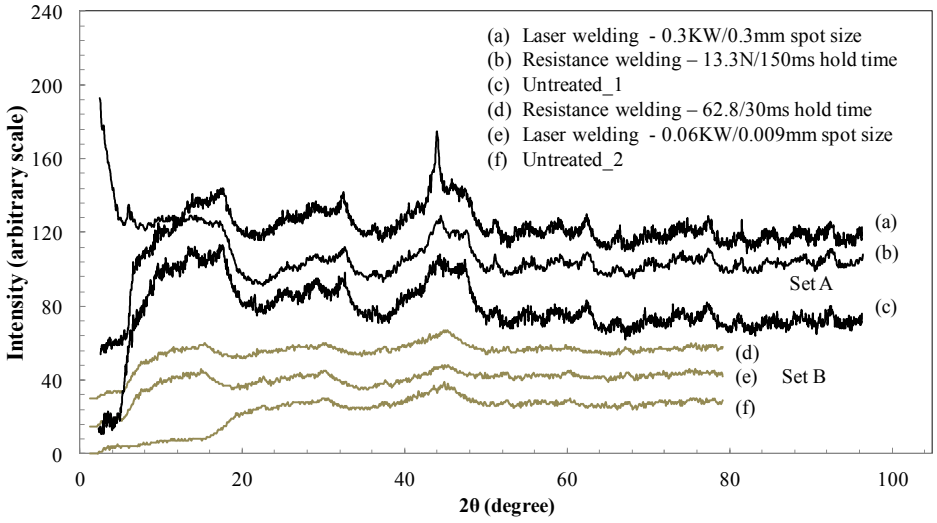

Figure 27 XRD results for resistance and laser welded amorphous $Fe_{45}Ni_{45}Mo_7B_3$ ribbons.

In contrast to welding results discussed so far, resistance welded samples under a 62 N force and a 30 ms hold time and the laser welded samples using a 0.06 KW power laser on a 0.009 mm spot size did not reveal signs of crystallization. XRD plots indicate no sharp peaks revealing a retained amorphous state. Resistance welded, pulsed laser weld and continuous laser weld samples showed no crystallization. When tested for their tensile lap joint shear strength, they showed a brittle failure compared to adhesives. Failure loads of resistance welds were 3.4 N for 4 spots, and the highest strength for a laser welded sample was 52.8 N for a 2.4mm^2 area. Laser welded lap joints exhibited the highest strength of 22 MPa in tension. However, welded samples failed in a brittle fashion upon bending.

Micrographs of laser welded regions of sample set-A are presented in Figure 28. In the pulsed laser welded sample shown in Figure 28 (f), there was thermal ablation. This process occurs as a result of surface vaporization caused by a localized increase in temperature. Smaller thermal diffusivities lead to efficient ablations. Thermal diffusivities of amorphous materials are on the order of 0.2 cm^2s^{-1} [79]. In pulsed laser welding, a long (6 ms) pulse duration was used, making thermal ablation unlikely [77]. However visible material removal features from micrographs remained suggestive.

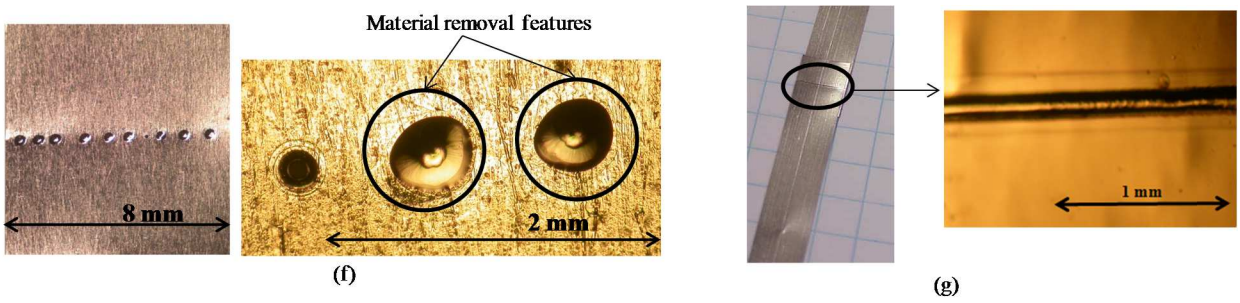

Figure 28 Microscopic observations: (f) pulsed laser weld across the amorphous $Fe_{45}Ni_{45}Mo_7B_3$ ribbon, (g) Continuous laser weld on the ribbon-ribbon interface.

Continuous wave laser welded samples show a straight line, which can be treated as a laser irradiated track which also failed in a brittle fashion. Their tensile lap joint shear strength was measured at 52.8 N; there were signs of embrittlement. Embrittlement effects have been postulated to occur due to structural relaxation involving short-range order accompanied by a reduced quenched-in free volume [80, 81]. A visible "ripple-like" formation was observed away from the laser irradiated line.

Table 7 Welding conditions and results

Type of welding	Condition	Result from XRD
Laser welding	0.3 KW, 0.3 mm spot size	crystallized
Resistance welding	13.3 N, 150 ms hold time	crystallized
Resistance welding	62.8 N, 30 ms hold time	amorphous
Laser welding	0.06 KW, 0.009 mm spot size	amorphous

2. Modified resistance welding using a chilled bath- Amorphous $Fe_{45}Ni_{45}Mo_7B_3$ ribbons were successfully welded using a modified cooling method. Increased cooling rate helped prevent crystallization and retain an amorphous weld. XRD results are shown for the two spot welds in the lap joint samples tested using condition 1: 22 N force, 3 ms, 0.6 kA. Samples A, B, C, D, and E refer to each of the 5 lap joint welded samples with two spot welds.

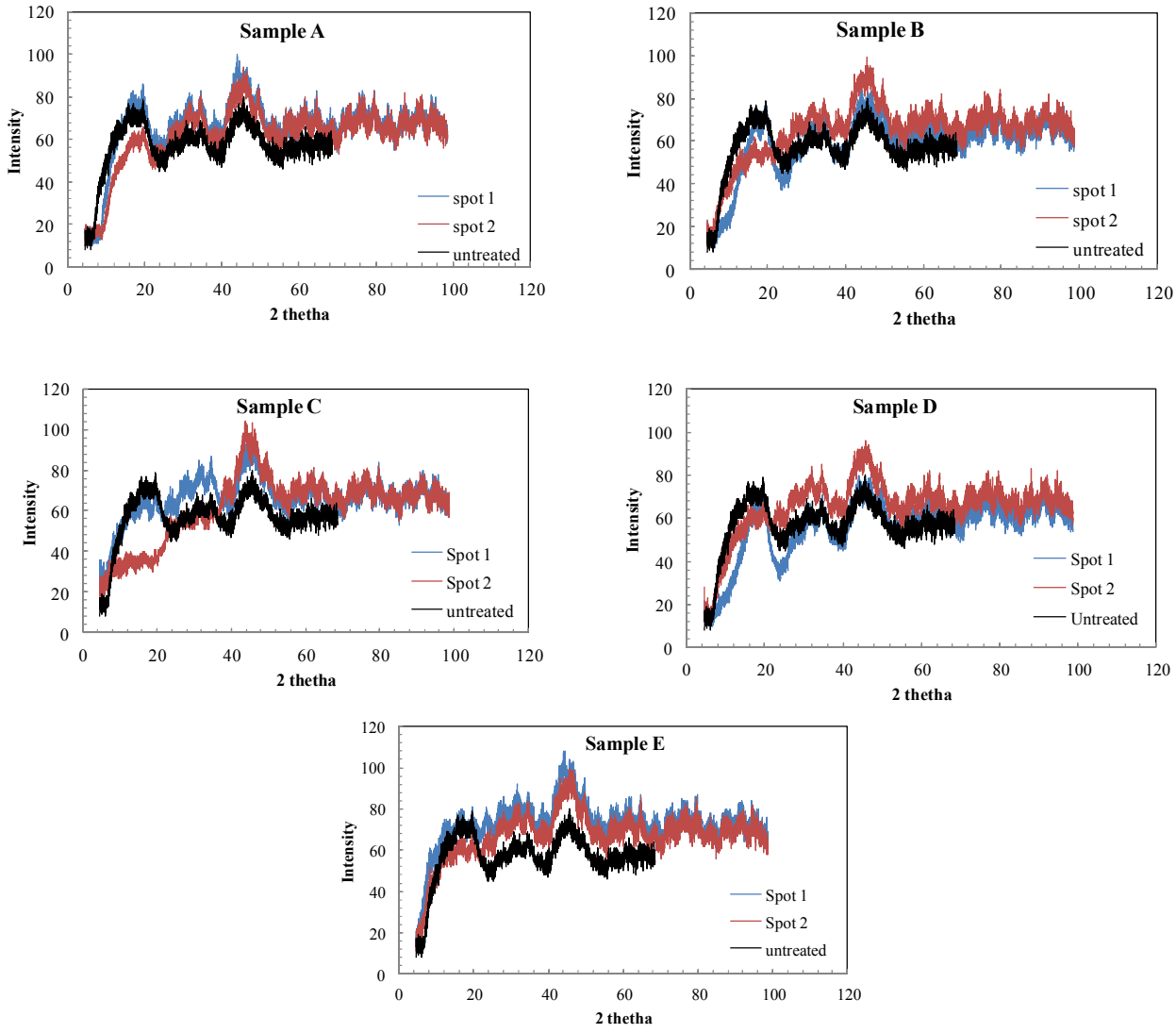

Figure 29 Plots from XRD measurements on welded amorphous $Fe_{45}Ni_{45}Mo_7B_3$ ribbons (with 2 spots). Unit for 2 thetha shown in x-axis is degrees.

Due to manual operation involved in welding individual spots, there were weld misalignments in some samples. This led to a bending moment while the sample was in tension, sometimes leading to pre-mature failure of one spot before another. Similar to samples with 2-spot welds, multiple spot weld samples had misalignment of weld spots across the weld axis. A similar failure pattern was observed. Reported values refer to the load recorded for failure of the first spot. Five samples were tested for lap joint strength.

Microscopic observations from sample S1 shows loss of material on one of the welded spots.

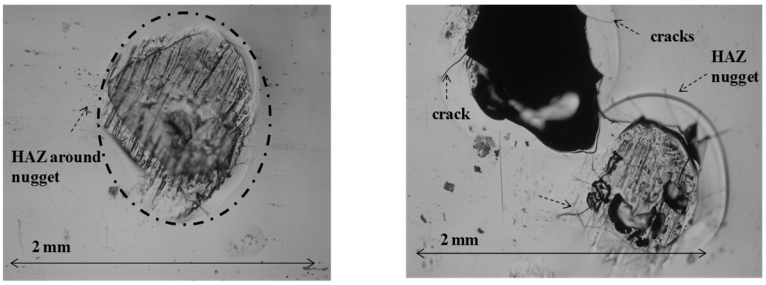

Figure 30 Microscopic observations of the multiple-spot welded samples, showing HAZ (left), loss of material in sample S1 and micro cracks that extend to the neighboring weld).

Also, HAZ was evident, showing micro-cracks emanating from welds. HAZ did not affect neighboring spot welds. In sample S4, a significant misalignment was seen on the tension testing axis caused by lap joint misalignment of ribbons during welding. This affected the apparent lap-joint strength as see in the results (Table 6).

From mechanical testing results, it is evident that welded amorphous $Fe_{45}Ni_{45}Mo_7B_3$ ribbons has a significantly higher lap joint shear strength compared to adhesives. Care is needed to align weld spots and achieve a constant cooling rate for all spots to maintain consistency.

3.6 Chapter Summary

For amorphous $Fe_{45}Ni_{45}Mo_7B_3$ ribbons, a minimum adhesive force to form a teardrop cell shape was calculated from experimental testing. It is shown to scale with the axial strength of the honeycomb, as cell size decreases. The force calculated from an elastic bending model validated the experimental trend and indicates that at a cell size of 2 mm, shear bands start. A successful welding method has been demonstrated to join amorphous

$Fe_{45}Ni_{45}Mo_7B_3$ ribbons. XRD studies on welded samples from the preferred method do not show signs of crystallization. Ribbons remained amorphous before and after the weld. By improving the cooling rate of the weld, crystallization has been avoided, maintaining the strength of the weld. Results from lap joint shear strength tests of modified spot welds show a 15 X improvement compared to adhesives. Increasing the number of spot welds does not affect weld strength to a limit of six weld spots across an 8 mm wide ribbon.

Methods proposed here provide a successful welding approach for joining metallic glasses without crystallization. Limited data on welding MG ribbons was found in the literature. Much attention has been on joining BMGs using laser welding, as an attempt to increase their length scales. Previous work on spot welding of Fe- based glassy ribbons, have shown crystallization from the slow cooling time, resulting in embrittlement of joints [61]. While modified spot welding showed a higher lap joint strength, weld alignment, cost, complexity of set-up and operation to use welding in manufacturing honeycombs with a "teardrop" cell shape should be considered. For structural applications involving inter-cellular joining of amorphous metal honeycombs, it is unfavorable to have a brittle bond between the cells.

The following chapter discusses an unusual method of forming teardrop cells by manipulation of residual stresses in amorphous ribbons.

CHAPTER IV

RESIDUAL STRESS FROM PEENING OF METALLIC GLASS

4.1 Introduction

In a 2011 lab discovery, a significant curvature was observed in amorphous $Fe_{45}Ni_{45}Mo_7B_3$ ribbon (50.4 mm wide, 29 µm thick) when exposed about 3 seconds to a stream of glass beads at 0.5 MPa (75 Psi) pressure. Upon varying pressure and time, it was found that a radius of curvature of approximately 1.5 mm can be achieved. This results in a local "teardrop" like shape in the ribbon. Custom fixtures and templates were designed and developed to use this process to manufacture "teardrop" celled honeycombs.

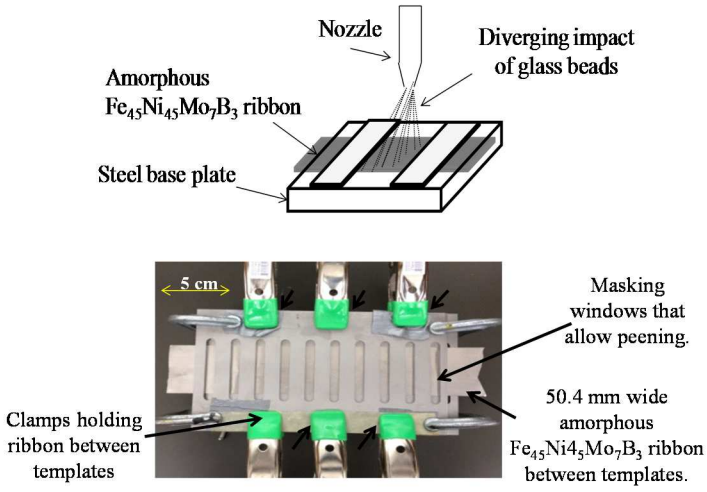

Figure 31 **Custom machined masking templates (left), 50.8 mm wide amorphous $Fe_{45}Ni_{45}Mo_7B_3$ precursor held in masking templates.**

Glass beads were blasted through windows of a masking template that exposed $Fe_{45}Ni_{45}Mo_7B_3$ alloy Amorphous Metal Ribbon (AMR) precursor. After removal from the template, the ribbon elastically curled toward the center to form multiple teardrop cells.

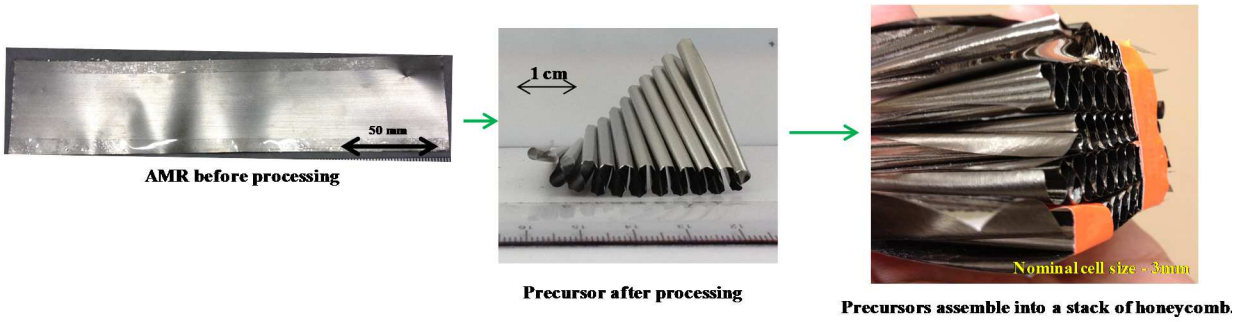

Figure 32 Photos of AMH precursor before and after processing.

Processed ribbons were stacked on one another to demonstrate a honeycomb with "teardrop" cells. Figure 32 show pictures of processed ribbons.

Residual stresses are expected in the manufacture of amorphous metal ribbons due to rapid solidification. Ribbon thickness also plays a role, so it is not clear how much of a stress gradient is quenched-in. Residual stresses result from surface chilling causing temperature gradients as the ribbon cools through glass transition [82, 83]. Two processes are used in manufacturing amorphous metal ribbons.

(1) Chilled Block Melt Spinning (CBMS), where a jet of liquid metal is ejected from a circular nozzle several mm away from the spinning wheel. Amorphous ribbons of width 1-20 mm are manufactured using CBMS.

(2) Planar Flow Casting (PFC), where rectangular nozzles with a smaller gap is used [83]. Widths of 50-200 mm are manufactured using PFC.

In both processes, non-uniform temperature distribution along ribbon thickness is predicted to cause high compressive residual stresses ($\sigma < 0$) near the surface facing cooling drum

and tensile residual stresses ($\sigma > 0$) on the free surface [84]. In manufacturing amorphous ribbons, due to nozzle distance, orientation, shape, and platen temperature, different quenched-in stress anisotropy and surface tension can be expected. These process variables influence atomic structure and physical properties [85, 86]. Quenched-in stresses depend on macroscopic and microscopic length scales. Surface or bulk defects on ribbons from different processes may also vary for the same reason. This is also evident from in-homogeneities of rapid quenching demonstrated using experimental procedures [87]. As a result, sizeable curvatures have been demonstrated with concavity towards the free surface. This is due to different solidification time taken by each successive layer in the ribbon. Homogeneous models have been developed to predict the curvature in as-quenched ribbons. Major curvatures have been postulated to result also from early solidification of edges due to a high cooling rate that adds compressive stresses in narrow ribbons using CBMS. Wider ribbons manufactured using PFC maintains the ribbon flat, owing to the weight of the puddle [88]. Measuring and understanding the magnitude and direction of these residual stresses is crucial in explaining their response to certain subsequent processing treatments. With an interest in increasing the general plasticity of Bulk Metallic Glasses (BMGs), shot peening as a surface treatment process has been studied [8, 89-92]. In certain BMG alloys, peening has been used to induce useful residual stresses to improve plasticity and fatigue limits.

This chapter investigates the response of amorphous $Fe_{45}Ni_{45}Mo_7B_3$ ribbons to shot peening using glass particles. Significant curvatures were observed as a result of peening. XRD measurements on peened ribbons were compared to untreated ribbons. Change in

curvatures and thicknesses were measured. Young's modulus and strength were measured and reported before and after peening.

4.2 Background

Thermal residual stresses are expected in metallic glasses due to the high cooling rates (10^6 K/s) required in their production to retain a liquid like atomic structure. Analytical models have been developed to predict residual stresses in Bulk Metallic Glasses (BMGs, a length scale of 1 cm or more) using an instant freezing model, supported by results from layer removal methods [82]. A major drawback of metallic glass is its near zero ductility in tension due to shear localization [8]. To improve plasticity and prevent catastrophic failure, the introduction of a second phase has been studied in processing BMG based composites [93-97]. For Bulk Metallic Glasses (BMGs), their visco-elastic nature, poor thermal conductivity and high freezing rates lead to compressive residual stresses on the surface and tensile stress in the interior. Substantial surface residual stresses (up to 900 MPa) have been shown also through analytical and Finite Element models [98]. Residual stresses have been considered detrimental in metallic glasses for several reasons including: the degradation of magnetic properties [99], interference with measurements of hardness [8], and altering fracture toughness [100]. However, introducing compressive residual stress in BMGs using indentation [101] and shot peening [8] were approaches sought for improving plasticity. Peening of a Zr -based BMG (Vitreloy 1) has shown a decrease in surface hardness, which was also correlated to the compressive residual stresses on the surface. A convex curvature was reported on a peened surface of a BMG plate [8]. In DSC measurements on peened Pd-based BMG, the thermal relaxation spectrum shifted to a lower temperature, suggesting that peening increases atomic mobility [90]. Studies on

peened Zr-based metallic glass plates [89] show maximum sub-surface compressive stresses close to the uniaxial yield stress of an un-deformed BMG. A change in bond orientation ordering is also observed due to plastic flow. Similar studies have indicated that the flexion on a shot peened surface and microstructural deformation increased with peening time or pressure. Interestingly, increasing shot-peening time or pressure did not increase residual stresses [91]. Compressive residual stresses have also shown to increase the fatigue cycles for crack initiation. [91]. There was no evidence of crystallization induced by peening found in literature. Characterizing the magnitude and depth of residual stresses and understanding their impact on mechanical properties is critical. Substrate curvatures have been used in measuring residual stresses in BMGs as a result of shot peening [8] also in tempered soda alumina silicate glasses [102]. A comparison of measured compressive residual stresses using different treatments and methods have been summarized in literature [89]. As a result of plastic deformation from peening, metallic glasses have also shown to change their atomic structure [89]. Bond orientation ordering and relaxation of glassy structure have been attributed to enhanced atomic mobility [90]. Other studies have attributed structural relaxation to cyclic elastic loading [103]. Measuring density is a direct method to show a change in free volume as a result of peening, but smaller processing-induced changes affect the measurement [104, 105]. Measurement and comparison of elastic moduli have also been suggested to understand changes in free volume [106].

4.3 Experimental Methods

Amorphous $Fe_{45}Ni_{45}Mo_7B_3$ ribbons of 29 μm thickness and 50.8 mm width were used in this study. Owing to surface chilling in the manufacture of the ribbon, ribbon surfaces

textures were different. Reflective on one side and matte on the other. Ribbon samples were peened on both sides under two conditions.

1. **Condition 1** – Shot peened by holding them between Stainless Steel 316 templates, similar to the set-up in Figure **31**.

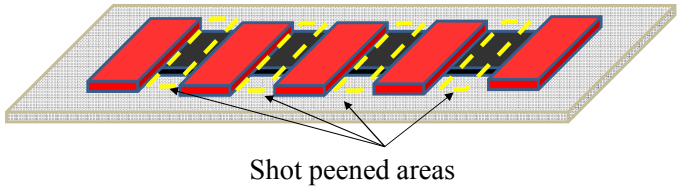

Figure 33 Peening using templates.

2. **Condition 2** – Shot peened by holding them on plates made of 50.8 mm wide Aluminum 2024, secured on a stainless steel base plate.

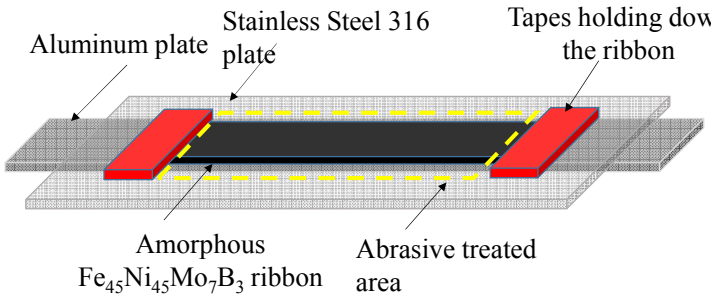

Figure 34 Peening with all of ribbon area exposed.

Condition 1 was used to observe multiple curvatures and demonstrate repeating teardrop shapes. *Condition 2* was used to evaluate the effect of peening when all of the ribbon area is exposed. The reflective side was treated first in both conditions followed by the matte side. Peening was performed in an enclosure[9] equipped with a reclaimer and a

[9] Zero INEX 3048R

dust bag. Glass beads of type BT-8 were used as impact media (0.15-0.2 mm in diameter). Several pressures were used from a 114±10 mm nozzle distance. Because a significant ribbon curvature was observed for a pressure of 0.5 MPa (75 psi), this pressure was considered for further study. Untreated and peened ribbons were etched using a 3% Nital solution to observe curvature changes. X-ray diffraction (XRD) measurements were conducted on ribbons before and after peening. X-ray diffraction[10] was performed with Cu-K_α radiation at tube parameters of 40kV/40mA. Detector distance to the center of diffraction was kept at 30 cm, which covers approximately an area of 20° in 2θ and 20° in χ with 0.02° resolution. A motorized five axis (X, Y, Z (translation), χ (tilt), φ (rotation)) stage was used to move the measurement spot to instrument center within a 12.5 μm position accuracy. Sample positioning was controlled by a video-laser positioning system before each exposure to ensure diffraction patterns come from the peened region. Samples for tension testing were prepared from peened ribbons of 8 mm width, peened using *Condition 1*. Samples using *Condition 2* were prepared from ribbons of 50.4 mm width. Four samples were prepared for bulk tension tests, shearing them from a 50.4 mm wide ribbon, with each sample of width 12.5 mm. Tension tests were performed using a hydraulic driven Instron UTM using ASTM[11]. Aluminum tabs were glued to ribbon test specimen ends to avoid slipping from the Instron grips. Applied strain was computed using a Laser Extensometer[12] and a data-logger suitable for recording compliance free strain measurements. Micrographs of the ribbon surface and thickness were taken using a field

[10] Bruker D8 Discover XRD^2 micro-diffractometer equipped with the General Area Diffraction Detection System (GADDS) and Hi-Star 2D area detector.
[11] ASTM E345 - 93(2008) "Standard Test Methods of Tension Testing of Metallic Foil"
[12] Model LE-05.

emission scanning electron microscope (FESEM)[13] equipped with a back scatter detector and EDAX system. The mass of ribbons to a 0.1 mg accuracy was measured before and after peening.

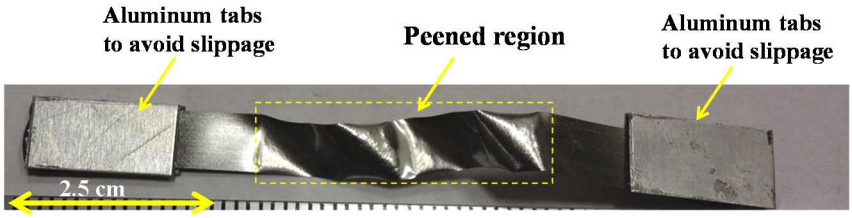

Figure 35 Tension testing sample, with peened region (using condition 1)

4.4 Results

Condition 1

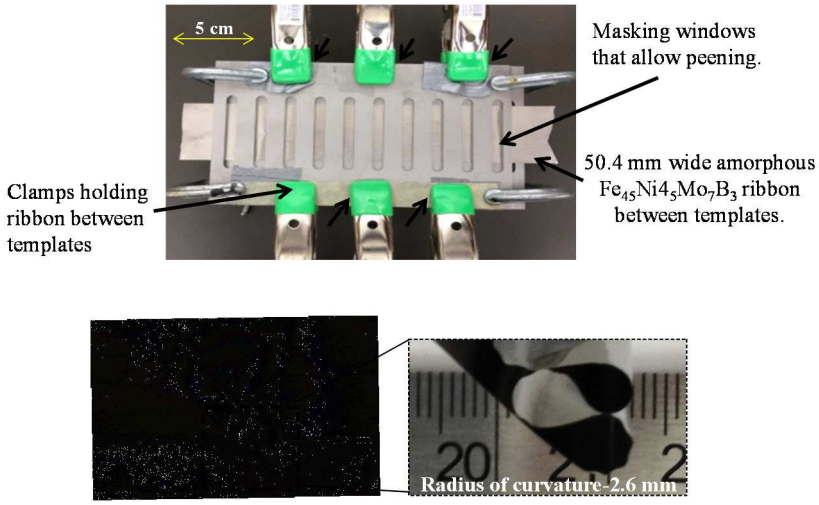

Figure 36 **Picture of ribbon in template before peening (top), top view pictures of peened ribbons after removal of templates.**

Condition 2

[13] Hitachi S4800-high resolution.

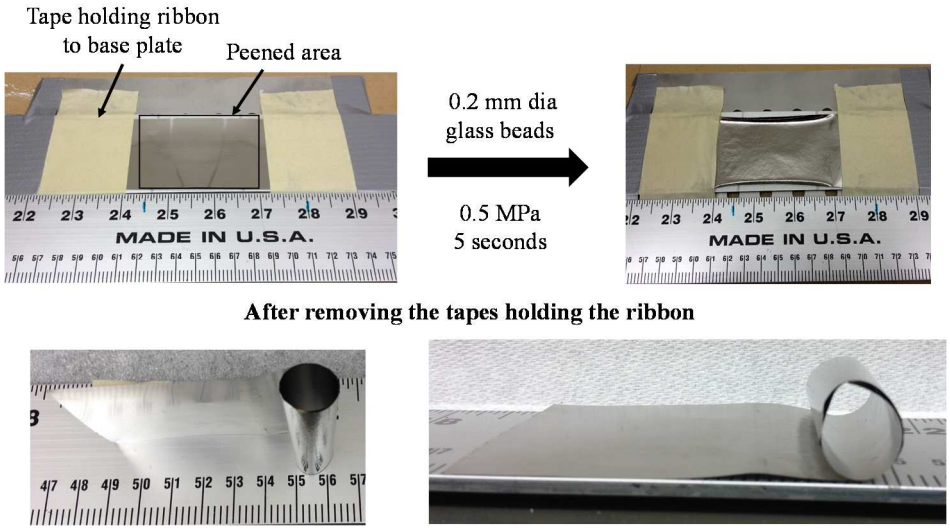

Figure 37 Pictures of ribbon before and after peening (top), top and side view pictures of peened ribbons after removal of tapes holding the ribbon to templates.

Upon removing boundary clamps from the template after peening, significant curvatures were observed. Changes in surface texture were also observed. Data from XRD measurements for untreated and peened conditions were collected. There were no signs of crystallization observed when comparing results from untreated and peened ribbons for the reflective side. XRD elastic strains can be calculated using Bragg's equation given by

$$\lambda = 2d \sin \theta \tag{11}$$

$$\varepsilon = \frac{d_f - d_i}{d_i} \tag{12}$$

λ is the wavelength of the Cu-Kα X-ray source (1.5Å), d the average lattice spacing, θ the diffracting angle, ε strain.

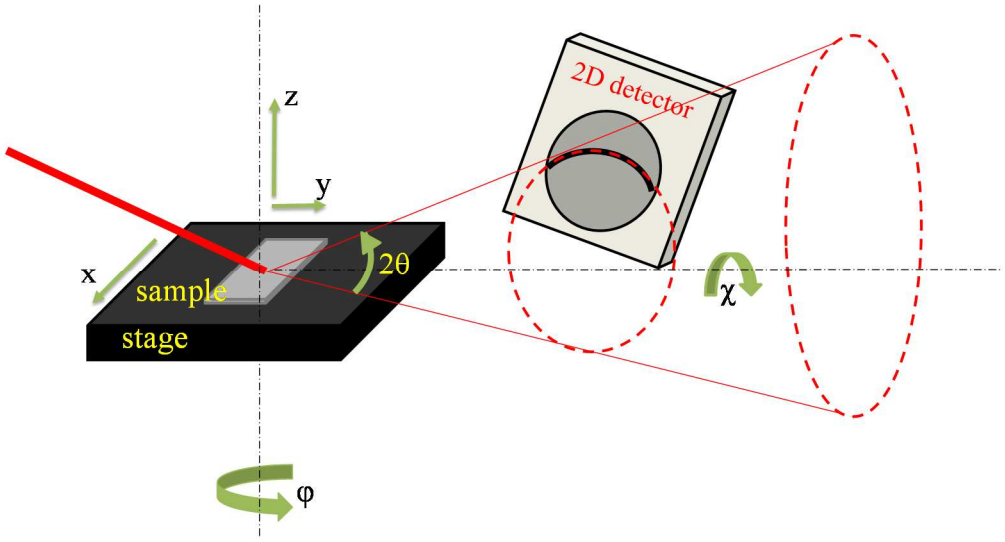

Figure 38 Schematic of sample set-up in diffractometer and resulting diffraction pattern.

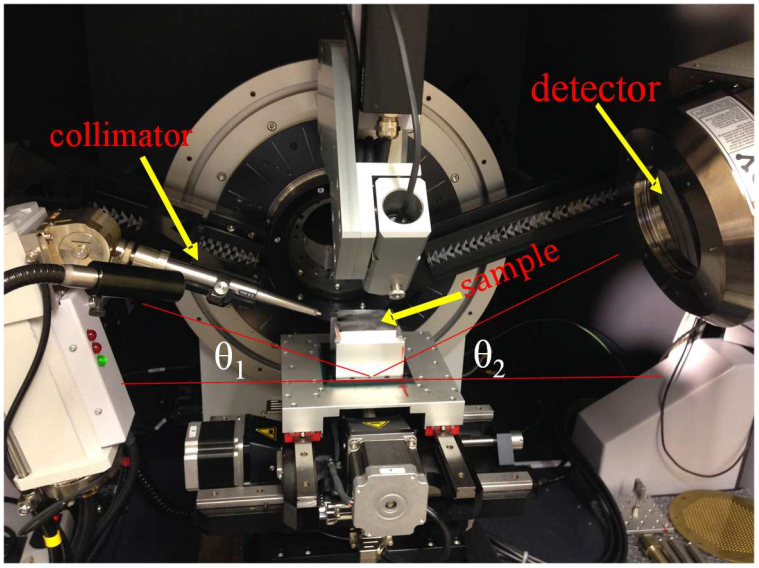

Figure 39 Picture of XRD set-up.

1D XRD data with 2θ (degrees) in the x-axis and intensity (arbitrary units) in the y-axis were plotted for treated and peened ribbons. Shown in Figure 40.

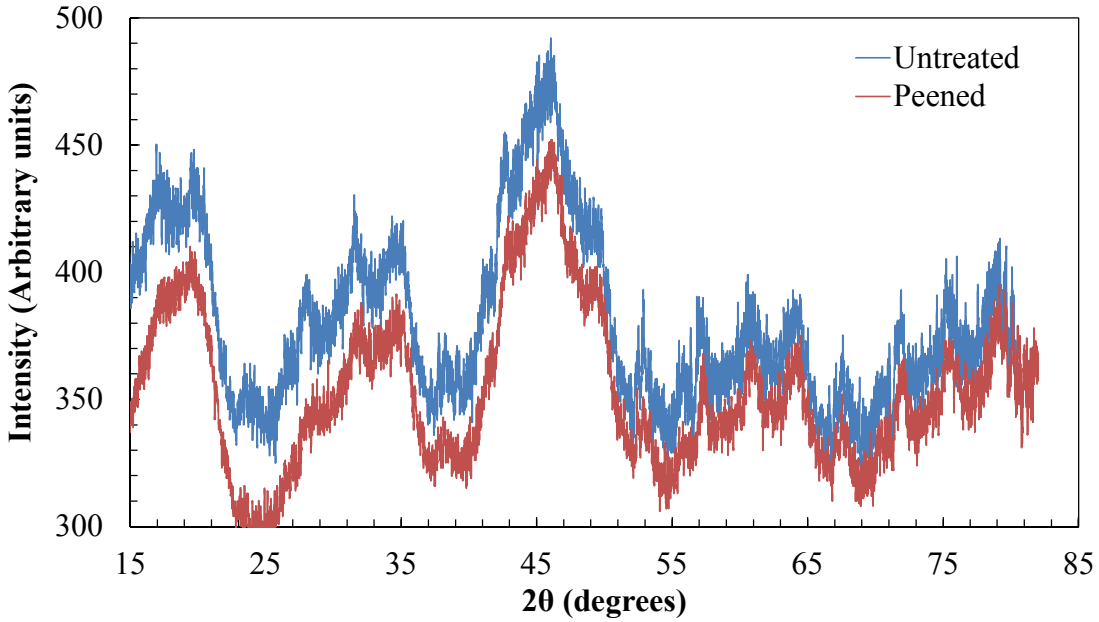

Figure 40 1D XRD data for untreated and peened ribbons. Some erroneous signal error from the detector limits the value of this data, but the concept remains useful.

In a 1D XRD pattern for typical crystalline materials, sharp peaks appear for a given diffraction angle θ which is related to d-spacing using Bragg's law. Amorphous metals do not coherently diffract x-rays. But, their 1D pattern as seen in Figure 40, show amorphous humps at certain 2θ angles, which can be related to average atomic spacing. When a significant shift in the center of the amorphous hump is expected, the corresponding change in average atomic spacing could be related to XRD elastic strains in the measured direction. To estimate the average peak center of an amorphous hump, a Gaussian function of the form:

$$y = y_o + \frac{A}{W\sqrt{\frac{\pi}{2}}} e\left(\frac{(-2(x-x_c))}{w}\right)^2 \tag{13}$$

where x_c is the peak center was used. An example of a Gaussian fit to the individual amorphous humps is shown in Figure 41. This shows a shift in x-center.

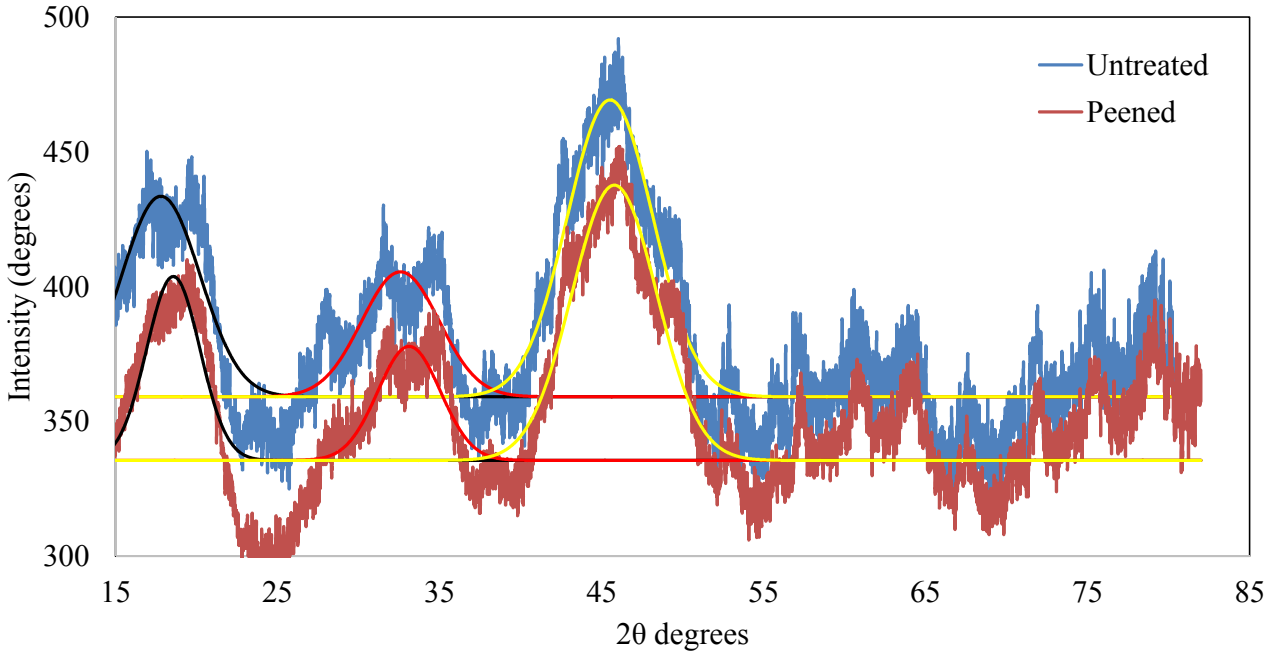

Figure 41 XRD peak pattern for untreated and peened samples. Gaussian peak fits (black, red and yellow thin lines) shown for each theta range.

Results from tension testing of peened ribbons (Using condition 1) with different areas of peening were compared to untreated ribbons. Yield strength and the Young's modulus were calculated from the resulting stress-strain data.

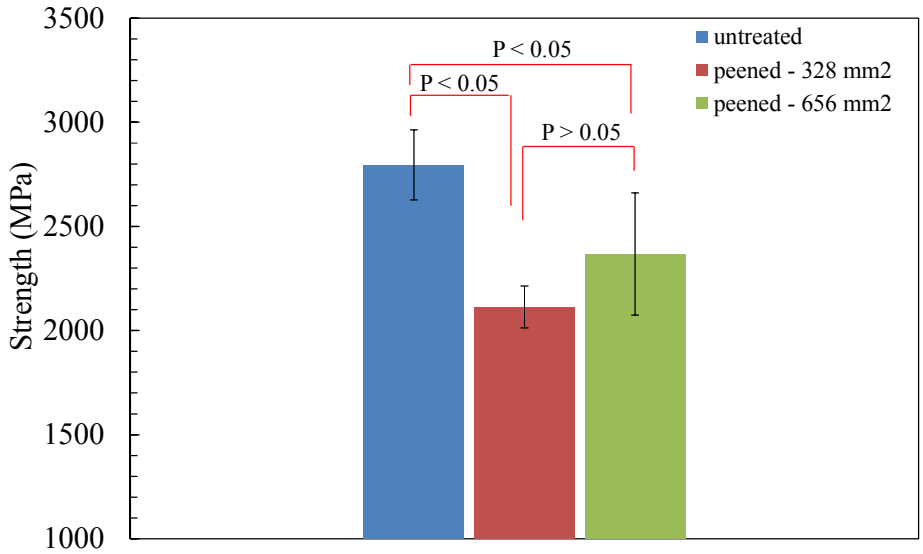

Figure 42 Yield Strength of untreated and peened ribbons. Error bars from Std. dev. (n = 5, 3, 3)

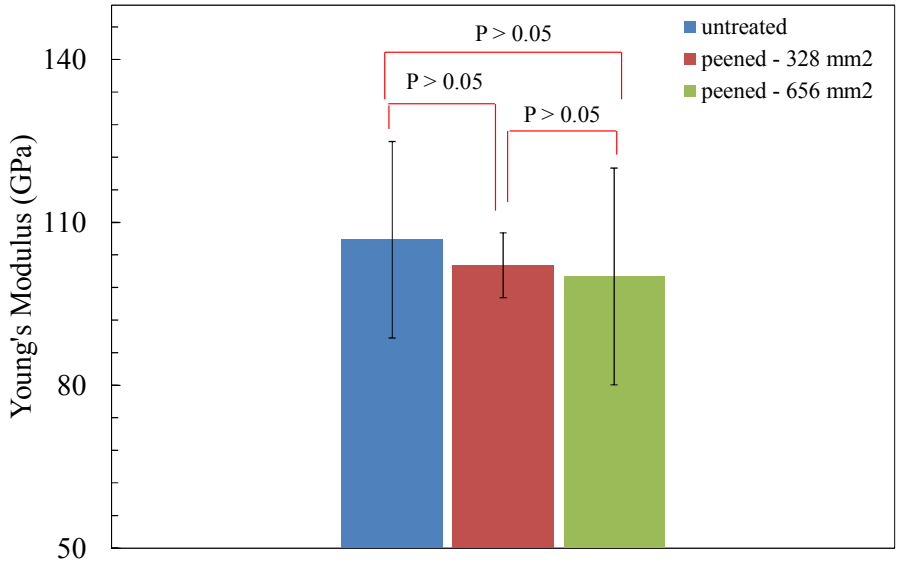

Figure 43 Young's modulus of untreated and peened ribbons. Error bars from Std. dev. (n = 5, 3, 3)

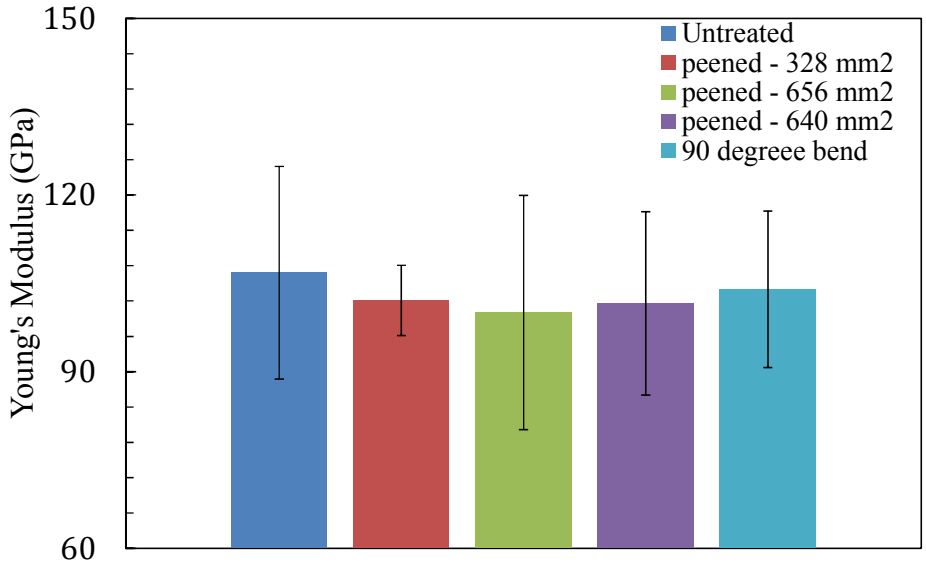

Figure 44 Comparison of Young's modulus measured from tension testing under different conditions. Error bars from std. dev (n = 5, 5, 3, 3, 3)

For samples peened using condition-1, there were untreated regions between peened regions that helped mount sample on Instron grips. Samples peened using condition 2 had

a tendency to warp because of the curvatures caused by peening. Some samples sheared near the grips, with failure initiating from to the micro-cracks seen on ribbon edges.

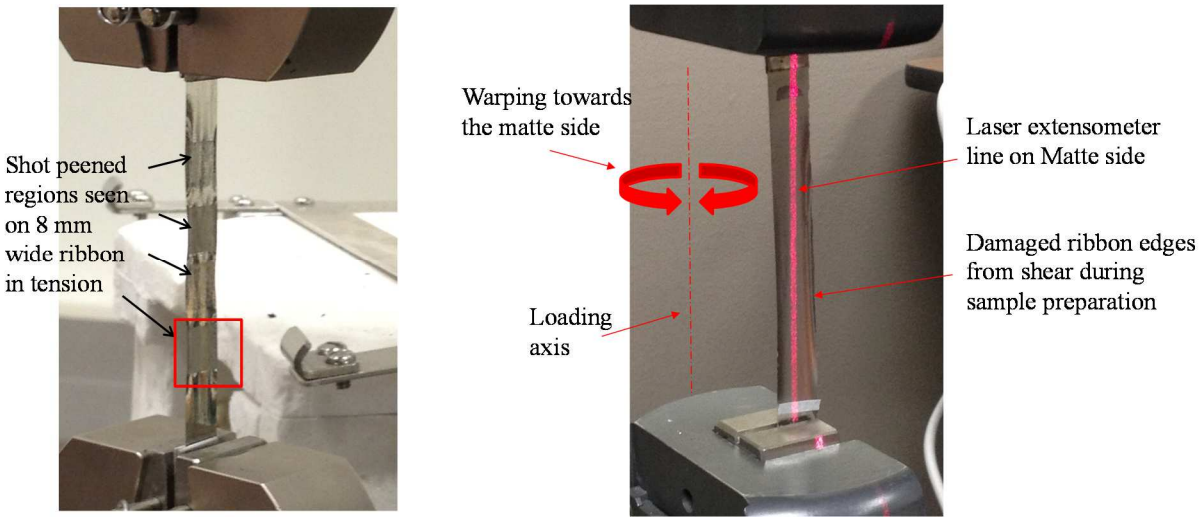

Figure 45 Picture of peened ribbon under tension. *Condition 1* (left) and *Condition 2* (right)

The mass of each ribbon sample was measured before and after peening. Results showed no difference for a ±0.1 mg measurement resolution. Thickness measurements from SEM micrographs show distortion on ribbon edges and a 10-17% reduction in edge thicknesses between treated and peened ribbons. This was confirmed by thickness measurements using X-ray µ-Computed tomography techniques. Note that the reported strength and Young's modulus values were calculated using the original thickness of 29 µm. With a 10% reduction in thickness, there were no significant differences seen on Young's modulus measurements.

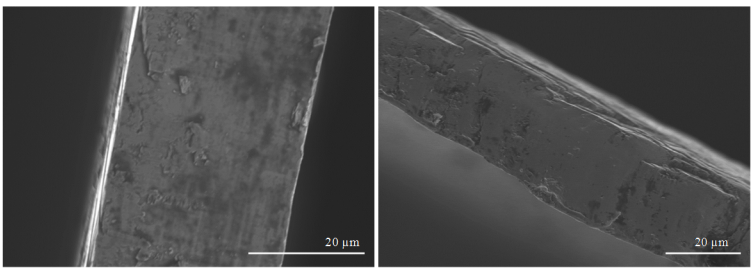

Figure 46 SEM micrographs of untreated (left) and peened (right) amorphous $Fe_{45}Ni_{45}Mo_7B_3$ ribbons; Note the reduction of thickness after impact, and the distorted edges. (Condition 1)

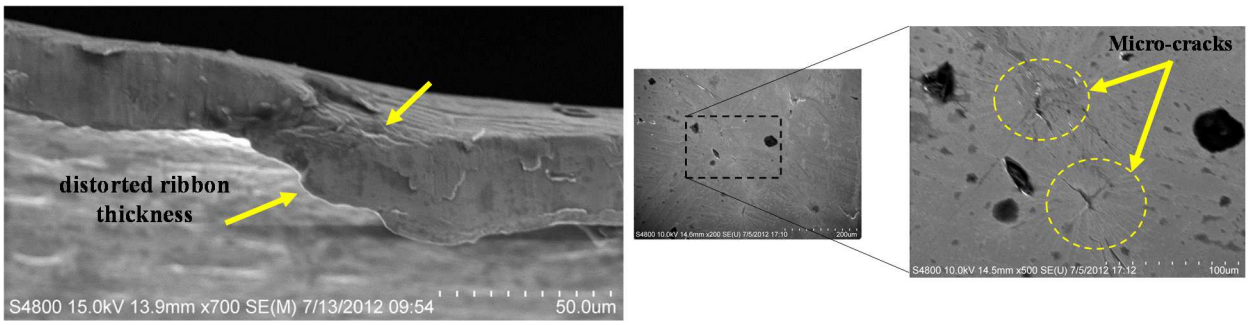

Figure 47 SEM micrographs showing damage area and cracks after peening

SEM micrographs on peened ribbon surface show regions of micro-cracks on the impacted surface (Figure 47). XRD measurements on peened ribbons show no signs of crystallization. This behavior is consistent with shot peened BMGs [90]. The formation of significant curvature upon impact is interesting. Ribbons manufactured both using CBMS and PFC have shown residual stresses from rapid quenching [83, 84, 87]. External processing such as peening, changes residual stress states on the ribbon, also changing ribbon curvature. As opposed to chemical etching, that would relieve compressive residual stress, peening imparts compressive residual stresses on ribbon surface. Stress states on free surfaces, contact surfaces, and ribbon edges also contribute to the observed curvatures.

4.5 Discussion

As in crystalline metals, peening induces residual stress in amorphous metals. Early work on peening BMGs have shown this and reported residual stresses up to 1800 MPa [89]. Change in curvature has also been shown in attempts to improve BMG plasticity [8, 92]. Prior work on metallic glass shot peening has been reported on metallic glasses in the bulk form (length scales of 1 cm or more) and not as ribbons. In this work, sizeable

curvatures are reported for different peening conditions for metallic glass ribbons of 29 μm thickness.

A drop in diffracted intensity was observed from 1D XRD data (Intensity Vs 2θ) of peened ribbons when compared to untreated ribbons. This can be partially attributed to change in surface roughness caused by peening, also obvious in SEM images. Data also shows that the ribbons remained amorphous before and after peening. This is consistent with earlier work on BMGs. Measuring a shift in amorphous humps is a potential method for estimating XRD elastic strains in amorphous ribbons. XRD elastic constants are needed to estimate the magnitude of residual stresses. The magnitude of displacement ($\Delta 2\theta$), peak fit, and sample errors should be carefully considered when using them with to calculate XRD elastic strains.

In metallic glasses, local shear band transformation requires free volume to allow atomic mobility [107]. Deformation is associated with bond arrangement. Elastic deformation is associated with bond length changes. Other work [107] using XRD on amorphous metals show bonding rearrangements in elastic and plastic deformation where bond exchange initiated deformation, while the total number of bonds remained unchanged. Bond orientation anisotropy has been reported as a result of local bond deformation measured in a mechanical creep study of metallic glasses [108]. Tempering of conventional glasses hinder crack imitation at the surface around an impact zone and have shown to increase bending strength [8]. BMGs benefit from compressive residual stresses for increasing both plasticity [8, 89] and fatigue limits [91]. MGs (this work) may also benefit from residual stresses. Atoms prefer to move when there is free volume, therefore a change in bond length and a change in free-volume can be related to density and elastic modulus, both of

which are material properties. The in-plane elastic modulus measured from bulk tension testing of peened and untreated amorphous $Fe_{45}Ni_{45}Mo_7B_3$ ribbons did not show a significant difference. A *t*-distribution was used in determining the statistical significance of mechanical testing results for a 95% confidence level. A 10- 17% reduction in ribbon thickness, measured from scanning electron micrographs was also seen on the curvature as a result of processing. This change in ribbon thickness could be accompanied by a change in ribbon length and width, to accommodate the energy from peening and conserve volume. However, bond length and free volume can also reduce as the thickness decreases. If most of the change in atomic arrangement was in the out of plane direction, perpendicular to peening. Anisotropic strains would result from peening.

Chemical etching of both untreated and peened amorphous $Fe_{45}Ni_{45}Mo_7B_3$ ribbons did not show a change in curvature, suggesting the peening causes the ribbon to attain a new equilibrium state. The magnitude of induced residual stresses could be calculated using XRD elastic constants for amorphous $Fe_{45}Ni_{45}Mo_7B_3$ ribbons. This requires stressing the ribbons a known amount and measuring the change in atomic spacing. This is part of ongoing work.

4.6 Chapter Summary

Significant curvatures were observed in amorphous $Fe_{45}Ni_{45}Mo_7B_3$ ribbons as a result of peening. While the prediction of a tempering state would imply a residual compressive surface stress upon layer removal, peening of amorphous ribbons showed an opposite response. The amorphous phase of peened ribbons on the reflective side remained, as evident from XRD data. Scanning electron micrographs show distorted ribbon edges and

thickness reduction of up to 17% from peening. Young's modulus and yield strength measured from bulk tension testing of the in-plane direction did not show a significant change.

CONCLUSIONS

In processing amorphous metals as honeycombs, the teardrop cellular structure is ideal to handle the high elastic limit (>2%). Similarly, the typically thin walls (t<0.03 mm) lends the honeycomb to a low *t*/*l* ratio, promoting elastic buckling as the dominant deformation mechanism in honeycomb cell walls. Using the newly proposed analytical model for teardrop celled honeycombs, an optimum MH design density exceeding the axial compressive strength of aluminum honeycombs was determined. Results from experimental testing honeycombs of multiple densities and from two amorphous alloys with different Young's moduli validated the model. As predicted, an unprecedented axial strength of 90 MPa for an AMH density of 0.6 Mg/m^3 was demonstrated. Using a higher modulus amorphous metal, even higher axial compressive strength was achievable at lower densities.

The model also suggests that improved inter-cellular bonding helps increase achievable strengths for a given density. Results here suggest such an improvement is possible using welding. In welding amorphous ribbons, a high cooling rate is important to retain the glassy state. Resistance spot welding of amorphous Fe-Ni based amorphous ribbons in a methanol and ice bath helped retain an amorphous state and achieve a successful weld. Measured strength using lap joint testing showed a 15 X improvement compared to adhesively bonded lap joints.

Shot Peening of amorphous Fe-Ni based ribbons resulted in significant ribbon curvatures. By manipulating the residual stress in the amorphous ribbon, a structure that resembles a teardrop cell shape was demonstrated. Peening causes a local change in atomic spacing in the amorphous metal. X-ray elastic constants are necessary to quantify the magnitude of residual stresses. Results from uniaxial tension testing of peened ribbons show no significant change in Young's modulus. A change in thickness was measured using scanning electron micrographs, and confirmed by X-ray transmission measurements. With no effect on Young's modulus, peening is a viable process for manufacture of amorphous metal honeycombs. Achievable curvatures, lack of adhesive mass, and the cost of welding makes peening a logical process to consider in AMH manufacture. In a sandwich panel, using honeycomb as a core material, some force could be provided by the face sheets bonded on the top and bottom of the core. However, for applications involving compression of AMH, inter-cellular and inter-row joining forces should be significant to resist the buckling loads under compression.

CHAPTER V

CLOSING REMARKS AND FURTURE WORK

Experimental results validate the proposed analytical model for the axial compressive strength of amorphous $Fe_{45}Ni_{45}Mo_7B_3$ honeycombs with a teardrop cellular structure. Adhesively bonded AMH with a density of 0.6 g/cc shows a unprecedented axial compressive strength compared to existing honeycombs in open literature. A theoretical transition between a maximum specific strength with aluminum honeycombs to a higher maximum for amorphous metal honeycombs is also suggested by the models. However, this transition has occurred even before reaching the predicted density. This has to do with several factors including the bonding between cells and the mass of the adhesive required.

The analytical model for axial compressive strength proposed in this work shows a dependence on the Young's modulus of the base material. Other amorphous alloys with higher Young's moduli motivates engineering honeycombs using other amorphous alloys [15, 27, 109].

Table 8 Comparison of predicted and measured compression strength. Predictions based on analytical models for hexagonal [23] and teardrop cells[33] .

Honeycomb type	Cell shape	Density (Mg/m^3)	Compression Strength (MPa)	
			Predicted	Measured
Amorphous $Fe_{45}Ni_{45}Mo_7B_3$	Teardrop	0.6	100	90.1
Aluminum 5056	Hexagon	0.4	60.3	50.4
Nanosteel	Teardrop	0.5	130.5	69
Amorphous $Fe_{53}Cr_{15}Mo_{14}Er_1C_{15}B_6$	Teardrop	0.4	245	-

AMH performance can be further maximized by taking advantage of their high yield strengths. Alloys, such as $Fe_{61}Mn_{10}Cr_4Mo_6Er_1C_{15}B_6$ and $Fe_{53}Cr_{15}Mo_{14}Er_1C_{15}B_6$ [3] are candidate honeycomb materials provided they can be processed as ribbons. Enabling plastic yield, taking advantage of the very high yield strengths in amorphous metals, by engineering a critical *t/l* ratio can only expand its potential.

The success of welding shown in this work on amorphous $Fe_{45}Ni_{45}Mo_7B_3$ furthers the achievable specific strength, by reducing adhesive. The high corrosion resistances in amorphous alloys are an added advantage, which are advantageous to AMH compared to existing honeycombs. ***Conventional honeycombs cannot bridge the mass penalty gap due to inherent restrictions***. *For example, welding cannot be used in Nomex honeycombs. Although Aluminum honeycombs can be welded, the base material will have to be treated with corrosion resistant coatings in order to resist severe environments. This leads to mass addition that does not contribute to the axial strength of the honeycomb.* Since the need for adhesive is removed or can be reduced, AMH can now be considered for high temperature environments as well.

The response of shot peening has been of interest for the resulting curvatures. Future work can be in using paired distribution functions (PDF), to predict a change in the nearest

neighbor distance. The absence of crystallinity and long range order in amorphous metals has restricted the use of conventional characterization methods. The curvature response of metallic glass to peening needs further understanding. Besides, the characterization of residual stresses in peened metallic glass, the direction and magnitude of the stresses is of interest. There may be a 2D stress state. Most of the bond length changes as a result of peening may be out-of-plane, which can be measured using a transmission method only possible at a synchrotron source. Other unusual methods including laser processing [110] and ball rolling has shown to impart similar curvatures in amorphous metal ribbons, expanding possibilities of discovering behavior of amorphous metals.

APPENDICES

Appendix I Manufacturing AMH using folding method.

Rail and the movable parts.

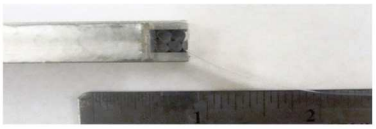

Top view during weaving , ribbon width is the height of the honeycomb.

A row of adhesively bonded row of amorphous lattice.

Bonded lattices to AMH.
Nominal cell size- 3 mm

Appendix II Manufacturing AMH with a cell size of 1.2 mm using the Weave and Comb method

Step 1: Select a weaving pin plate with holes equal to that of cell size and pins of similar diameter.

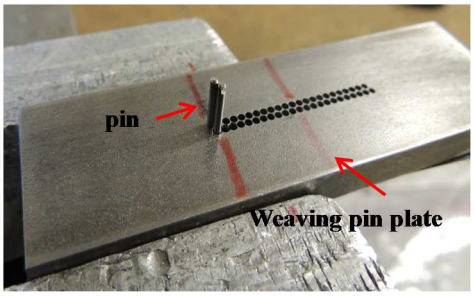

Step 2: Amorphous foils of required length wound around pins and completed woven foil held in a “teardrop” shape supported by pins.

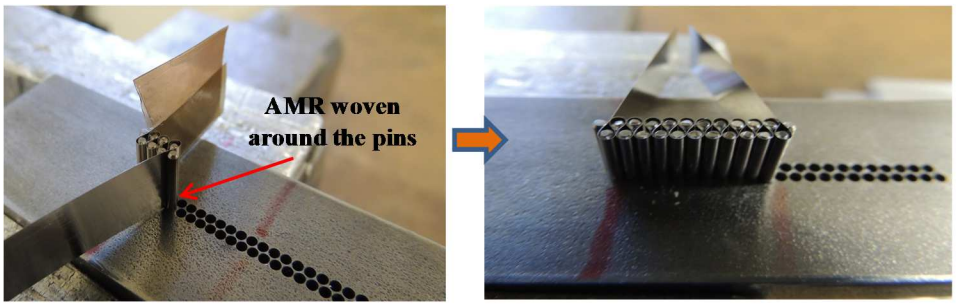

Step 3: Clamping fixture holding the woven teardrop row on the outside.

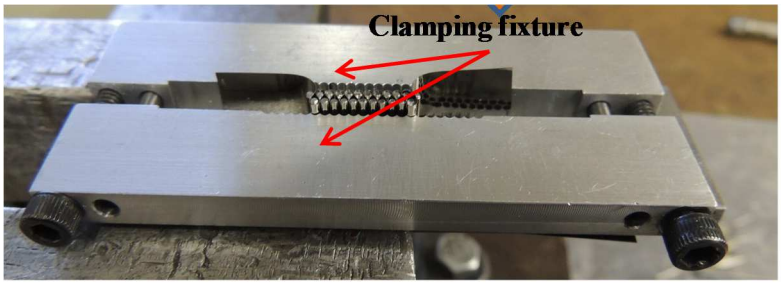

Step 4: Stabilizing combs inserted in the foil stick to hold cells in shape for clamping fixture to be released.

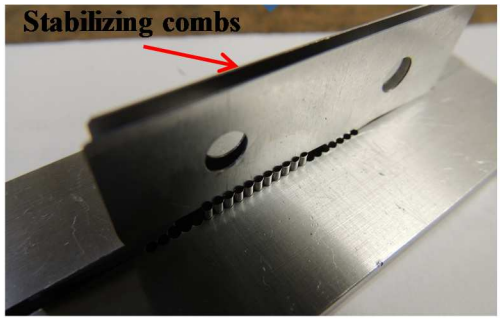

Step 5: Both ends of foils stick stabilized using combs on both sides.

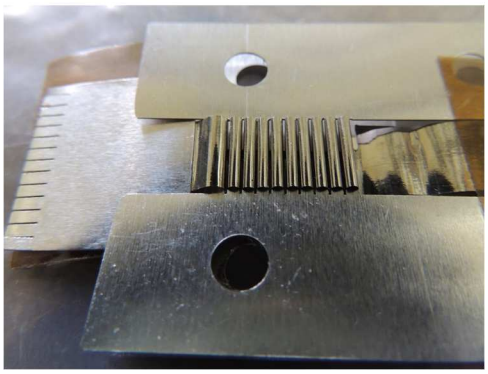

Step 6: Stabilized foil sticks stacked and ready for bonding cycle. Completed sample post-curing is shown in Figure 10.

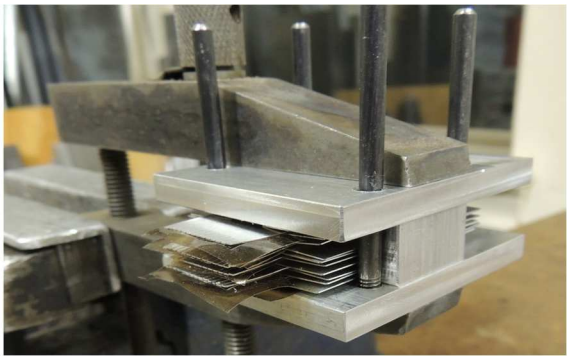

REFERENCES

[1] W. Klement, R. H. Willens, and P. Duwez, "Non-crystalline Structure in Solidified Gold-Silicon Alloys," *Nature,* vol. 187, pp. 869-870, 1960.

[2] M. Chen, "Mechanical Behavior of Metallic Glasses: Microscopic Understanding of Strength and Ductility," *Annual Review of Materials Research,* vol. 38, pp. 445-469, 2008.

[3] W. L. Johnson and K. Samwer, "A universal criterion for plastic yielding of metallic glasses with a (T/T-g)(2/3) temperature dependence," *Physical Review Letters,* vol. 95, Nov 2005.

[4] K. P. Koo and G. H. Sigel, "Characteristics of fiber-optic magnetic-field sensors employing metallic glasses," *Optics Letters,* vol. 7, pp. 334-336, 1982/07/01 1982.

[5] F. Bucholtz, K. P. Koo, A. M. Yurek, J. A. McVicker, and A. Dandridge, "Preparation of amorphous metallic glass transducers for use in fiber optic magnetic sensors," *Journal of Applied Physics,* vol. 61, pp. 3790-3792, 1987.

[6] V. R. V. Ramanan, "Metallic glasses in distribution transformer applications: An update," *Journal of Materials Engineering,* vol. 13, pp. 119-127, 1991/06/01 1991.

[7] A. Conroy, P. Georgopolos, and T. Rybak, "Bulk metallic glass motor and transformer parts and method of manufacture," ed: Google Patents, 2000.

[8] Y. Zhang, W. H. Wang, and A. L. Greer, "Making metallic glasses plastic by control of residual stress," *Nat Mater,* vol. 5, pp. 857-860, 2006.

[9] Z. G. Li, X. Hui, C. M. Zhang, and G. L. Chen, "Formation of Mg–Cu–Zn–Y bulk metallic glasses with compressive strength over gigapascal," *Journal of Alloys and Compounds,* vol. 454, pp. 168-173, 4/24/ 2008.

[10] X. L. Zhang, G. Y. Sun, and G. Chen, "Improving the strength and the toughness of Mg-based bulk metallic glass by Bridgman solidification," *Materials Science and Engineering: A,* vol. 564, pp. 158-162, 3/1/ 2013.

[11] D. C. Hofmann, "Bulk Metallic Glasses and Their Composites: A Brief History of Diverging Fields," *Journal of Materials,* vol. 2013, p. 8, 2013.

[12] A. H. Brothers and D. C. Dunand, "Plasticity and damage in cellular amorphous metals," *Acta Materialia,* vol. 53, pp. 4427-4440, 9// 2005.

[13] J. Schroers, C. Veazey, M. D. Demetriou, and W. L. Johnson, "Synthesis method for amorphous metallic foam," *Journal of Applied Physics,* vol. 96, pp. 7723-7730, 2004.

[14] T. Wada and A. Inoue, "Formation of Porous Pd-based Bulk Glassy Alloys by a High Hydrogen Pressure Melting-Water Quenching Method and Their Mechanical Properties," *Materials Transactions,* vol. 45, pp. 2761-2765, 2004.

[15] M. D. Demetriou, J. C. Hanan, C. Veazey, M. Di Michiel, N. Lenoir, E. Üstündag, *et al.*, "Yielding of Metallic Glass Foam by Percolation of an Elastic Buckling Instability," *Advanced Materials,* vol. 19, pp. 1957-1962, 2007.

[16] M. D. Demetriou, J. P. Schramm, C. Veazey, W. L. Johnson, J. C. Hanan, and N. B. Phelps, "High porosity metallic glass foam: A powder metallurgy route," *Applied Physics Letters,* vol. 91, 2007.
[17] J. C. Hanan, W. L. Johnson, and A. Peker, "Advanced Metal Foam Lunar Habitats and Structures.," *NASA NTR-41102,* 2005.
[18] J. C. Hanan and W. L. Johnson, "Amorphous Metal Improving Performance and Deployment of Solar Sails," *Advanced Space Propulsion Workshop,* 2004.
[19] J. C. Hanan, M. D. Demetriou, C. Veazey, F. DeCarlo, and J. S. Thompson, "Microtomotraphy of Amorphous Metal During Thermo-Plastic Foaming," *Adv. X-Ray Anal.,* vol. 49, pp. 85-91, 2006.
[20] H. M. Chiu, G. Kumar, J. Blawzdziewicz, and J. Schroers, "Thermoplastic extrusion of bulk metallic glass," *Scripta Materialia,* vol. 61, pp. 28-31, 2009.
[21] R. C. Sekol, G. Kumar, M. Carmo, F. Gittleson, N. Hardesty-Dyck, S. Mukherjee*, et al.*, "Bulk Metallic Glass Micro Fuel Cell," *Small,* vol. 26, p. 201201647, 2012.
[22] G. Kumar, J. Blawzdziewicz, and J. Schroers, "Controllable nanoimprinting of metallic glasses: effect of pressure and interfacial properties," *Nanotechnology,* vol. 24, pp. 0957-4484, 2013.
[23] L. J. Gibson and M. F. Ashby, *Cellular Solids: Structure and Properties* vol. 2: Cmbridge University Press, 1999.
[24] J. C. Hanan, B. Jayakumar, and A. Bhat, "Mechanical Properties of Amorphous Metal Honeycombs for Ballistic Applications," *ASME Conference Proceedings,* vol. 2009, pp. 73-74, 2009.
[25] M. F.Ashby, *Materials Selection in Mechanical Design*: Pergamon press 2005.
[26] Hexcel, "Honeycomb Data Sheets," Dec 2006 ed: HexCel Corporation.
[27] B. Sarac, J. Ketkaew, D. O. Popnoe, and J. Schroers, "Honeycomb Structures of Bulk Metallic Glasses," *Advanced Functional Materials,* vol. 22, pp. 3161-3169, 2012.
[28] L. Meza and J. Greer, "Mechanical characterization of hollow ceramic nanolattices," *Journal of Materials Science,* vol. 49, pp. 2496-2508, 2014/03/01 2014.
[29] B. Jayakumar, "Metallic Glass Honeycombs and Composite Body Armor," M.S. Thesis, Mechanical and Aerospace Engineering, Oklahoma State University, 2009.
[30] Hexcel, "Mechanical properties of HexCel honeycomb material," HexCel Corporation, C.A1986.
[31] M. G. Bhat A., Luo H., Lu H.B, Hanan J.C, "Dynamic Compressive Behavior of Fe-based Amorphous Metal Honeycomb," presented at the TMS, San Diego, CA, 2011.
[32] M. J. Silva and L. J. Gibson, "The effects of non-periodic microstructure and defects on the compressive strength of two-dimensional cellular solids," *International Journal of Mechanical Sciences,* vol. 39, pp. 549-563, 1997.
[33] B. Jayakumar and J. Hanan, "Modeling the Axial Mechanical Response of Amorphous $Fe_{45}Ni_{45}Mo_7B_3$ Honeycombs," *Metallurgical and Materials Transactions A,* vol. 43, pp. 2669-2675, 2012.
[34] H. Lee, S. Hong, J. Lee, and Y. Kim, "Mechanical behavior and failure process during compressive and shear deformation of honeycomb composite at elevated

temperatures," *Journal of Materials Science,* vol. 37, pp. 1265-1272, 2002/03/01 2002.

[35] M. Ashby and R. Medalist, "The mechanical properties of cellular solids," *Metallurgical and Materials Transactions A,* vol. 14, pp. 1755-1769, 1983.

[36] J. Zhang and M. F. Ashby, "The out-of-plane properties of honeycombs," *International Journal of Mechanical Sciences,* vol. 34, pp. 475-489, 1992.

[37] A. G. Evans, J. W. Hutchinson, N. A. Fleck, M. F. Ashby, and H. N. G. Wadley, "The topological design of multifunctional cellular metals," *Progress in Materials Science,* vol. 46, pp. 309-327, 2001.

[38] W. J. Stronge and V. P. W. Shim, "Microdynamics of Crushing in Cellular Solids," *Journal of Engineering Materials and Technology,* vol. 110, pp. 185-190, 1988.

[39] E. Wu and W.-S. Jiang, "Axial crush of metallic honeycombs," *International Journal of Impact Engineering,* vol. 19, pp. 439-456, 1996.

[40] W. Miller, C. W. Smith, and K. E. Evans, "Honeycomb cores with enhanced buckling strength," *Composite Structures,* vol. 93, pp. 1072-1077, Feb 2011.

[41] A. Fazekas, R. Dendievel, L. Salvo, and Y. Bréchet, "Effect of microstructural topology upon the stiffness and strength of 2D cellular structures," *International Journal of Mechanical Sciences,* vol. 44, pp. 2047-2066, 2002.

[42] K. Li, X. L. Gao, and J. Wang, "Dynamic crushing behavior of honeycomb structures with irregular cell shapes and non-uniform cell wall thickness," *International Journal of Solids and Structures,* vol. 44, pp. 5003-5026, 2007.

[43] D. H. Chen and S. Ozaki, "Stress concentration due to defects in a honeycomb structure," *Composite Structures,* vol. 89, pp. 52-59, 2009.

[44] E. C. Mellquist and A. M.Waas, "Size efffects in the crushing of honeycomb structures," in *45th AIAA/ASME/ASCE/AHS/ASC Structures, Structural Dynamics and Materials Conference*, Palm Springs, CA, 2004.

[45] S. Deqiang, Z. Weihong, and W. Yanbin, "Mean out-of-plane dynamic plateau stresses of hexagonal honeycomb cores under impact loadings," *Composite Structures,* vol. 92, pp. 2609-2621, 2010.

[46] S. Torquato, L. V. Gibiansky, M. J. Silva, and L. J. Gibson, "Effective mechanical and transport properties of cellular solids," *International Journal of Mechanical Sciences,* vol. 40, pp. 71-82, 1998.

[47] A.-J. Wang and D. L. McDowell, "In-Plane Stiffness and Yield Strength of Periodic Metal Honeycombs," *Journal of Engineering Materials and Technology,* vol. 126, pp. 137-156, 2004.

[48] R. K. Mc Farland, Jr., "Hexagonal cell structures under post-buckling axial load," *American Institute of Aeronautics and Astronautics,* vol. 1, p. 5, 1963.

[49] T. Wierzbicki, "Crushing analysis of metal honeycombs," *International Journal of Impact Engineering,* vol. 1, pp. 157-174, 1983.

[50] Y. Wang, "Elastic collapse of honeycombs under out-of-plane pressure," *International Journal of Mechanical Sciences,* vol. 33, pp. 637-644, 1991.

[51] B. Kim and R. M. Christensen, "Basic two-dimensional core types for sandwich structures," *International Journal of Mechanical Sciences,* vol. 42, pp. 657-676, 2000.

[52] W. Abramowicz, "The effective crushing distance in axially compressed thin-walled metal columns," *International Journal of Impact Engineering,* vol. 1, pp. 309-317, 1983.
[53] F. Côté, V. S. Deshpande, N. A. Fleck, and A. G. Evans, "The out-of-plane compressive behavior of metallic honeycombs," *Materials Science and Engineering: A,* vol. 380, pp. 272-280, 8/25/ 2004.
[54] W. Abramowicz and N. Jones, "Dynamic progressive buckling of circular and square tubes," *International Journal of Impact Engineering,* vol. 4, pp. 243-270, 1986.
[55] W. C. Young and R. G. Budiyanas, *Roark's Formulas for Stress and Strain*: McGraw-Hill, 2002.
[56] G. Gerard and H. Becker, *Handbook of Structural Stability*: NACA TN 1957.
[57] G. R. Mahadevan, "Characterization and Elimination of Defects in Metallic Glass Honeycombs," (M.S Thesis, Oklahoma State University, 2011).
[58] B. A. Hanan J.C., Mahadevan R.G, "Dynamic Compressive Behavior of Fe Based Amorphous Metal Honeycomb Cellular Structures," presented at the TMS, San Diego, CA, 2011.
[59] D. Runcev and L. Dorn, "Welding of cobalt-iron-based amorphous alloy foils with Nd:YAG laser," 2004, pp. 449-455.
[60] Y. Kawamura and Y. Ohno, "Superplastic bonding of bulk metallic glasses using friction," *Scripta Materialia,* vol. 45, pp. 279-285, 2001.
[61] S. Fukushima, "Spot welding of amorphous alloys," *Welding International,* vol. 5, pp. 654-659, 1991/01/01 1991.
[62] J. H. Kim, C. Lee, D. M. Lee, J. H. Sun, S. Y. Shin, and J. C. Bae, "Pulsed Nd : YAG laser welding of $Cu_{54}Ni_6Zr_{22}Ti_{18}$ bulk metallic glass," *Materials Science and Engineering a-Structural Materials Properties Microstructure and Processing,* vol. 449, pp. 872-875, Mar 25 2007.
[63] H. S. Wang, H. G. Chen, J. S. C. Jang, and M. S. Chiou, "Combination of a Nd:YAG laser and a liquid cooling device to $(Zr_{53}Cu_{30}Ni_9Al_8)Si_{0.5}$ bulk metallic glass welding," *Materials Science and Engineering: A,* vol. 528, pp. 338-341, 11/25/ 2010.
[64] T. Shoji, Y. Kawamura, and Y. Ohno, "Joining of $Zr_{41}Be_{23}Ti_{14}Cu_{12}Ni_{10}$ bulk metallic glasses by a friction welding method," *Materials Transactions,* vol. 44, pp. 1809-1816, Sep 2003.
[65] T. Shoji, Y. Kawamura, and Y. Ohno, "Friction welding of bulk metallic glasses to different ones," *Materials Science and Engineering: A,* vol. 375-377, pp. 394-398, 2004.
[66] Y. Kawamura and Y. Ohno, "Successful electron-beam welding of bulk metallic glass," *Materials Transactions,* vol. 42, pp. 2476-2478, Nov 2001.
[67] Y. Kawamura and Y. Ohno, "Spark welding of $Zr_{55}Al_{10}Ni_5Cu_{30}$ bulk metallic glasses," *Scripta Materialia,* vol. 45, pp. 127-132, 2001.
[68] Y. Yokoyama, N. Abe, K. Fukaura, T. Shinohara, and A. Inoue, "Electron beam welding of $Zr_{50}Cu_{30}Ni_{10}Al_{10}$ bulk glassy alloys," *Materials Transactions,* vol. 43, pp. 2509-2515, Oct 2002.

[69] Y. Kawamura, S. Kagao, and Y. Ohno, "Electron beam welding of Zr-based bulk metallic glass to crystalline Zr metal," *Materials Transactions,* vol. 42, pp. 2649-2651, Dec 2001.
[70] Y. Kim, D. Bourell, and C. Persad, "Consolidation of metallic glass ribbons using electric discharge welding," *Metallurgical and Materials Transactions A,* vol. 19, pp. 1634-1638, 1988.
[71] D. V. Louzguine-Luzgin, G. Q. Xie, T. Tsumura, H. Fukuda, K. Nakata, H. M. Kimura*, et al.*, "Structural investigation of Ni–Nb–Ti–Zr–Co–Cu glassy samples prepared by different welding techniques," *Materials Science and Engineering: B,* vol. 148, pp. 88-91, 2008.
[72] Y. Kawamura and Y. Ohno, "Metallurgical bonding of bulk metallic glasses," *Materials Transactions,* vol. 42, pp. 717-719, Apr 2001.
[73] J. Kim, D. Lee, S. Shin, and C. Lee, "Phase evolution in $Cu_{54}Ni_6Zr_{22}Ti_{18}$ bulk metallic glass Nd:YAG laser weld," *Materials Science and Engineering: A,* vol. 434, pp. 194-201, 10/25/ 2006.
[74] B. Li, Z. Y. Li, J. G. Xiong, L. Xing, D. Wang, and Y. Li, "Laser welding of $Zr_{45}Cu_{48}Al_7$ bulk glassy alloy," *Journal of Alloys and Compounds,* vol. 413, pp. 118-121, 3/9/ 2006.
[75] T. Tsumura and K. Nakata, "Laser welding of Ni-based metallic glass foil," *Welding International,* vol. 25, pp. 491-496, 2011/07/01 2011.
[76] J. Kim, D. Lee, S. Shin, and C. Lee, "Phase evolution in $Cu_{54}Ni_6Zr_{22}Ti_{18}$ bulk glass Nd : YAG laser weld," *Materials Science and Engineering a-Structural Materials Properties Microstructure and Processing,* vol. 434, pp. 194-201, Oct 25 2006.
[77] S. P. Harimkar, S. R. Paital, G. Wang, P. K. Liaw, and N. B. Dahotre, "Periodically Laser Patterned Fe-B-Si Amorphous Ribbons: Phase Evolution and Mechanical Behavior," *Advanced Engineering Materials,* vol. 13, pp. 955-960, 2011.
[78] S. Katakam, J. Y. Hwang, H. Vora, S. P. Harimkar, R. Banerjee, and N. B. Dahotre, "Laser-induced thermal and spatial nanocrystallization of amorphous Fe–Si–B alloy," *Scripta Materialia,* vol. 66, pp. 538-541, 2012.
[79] H. S. Chen, H. J. Leamy, and C. E. Miller, "Preparation of Glassy Metals," *Annual Review of Materials Science,* vol. 10, pp. 363-391, 1980.
[80] E. T, "Structural relaxation in amorphous alloys - compositional short range ordering," *Materials Research Bulletin,* vol. 13, pp. 557-562, 1978.
[81] Y. Takahara and H. Matsuda, "Reversible structural relaxation in Fe-B-Si amorphous alloys," *Materials Science and Engineering: A,* vol. 179–180, Part 1, pp. 279-282, 1994.
[82] C. C. Aydiner, E. Üstündag, and J. C. Hanan, "Thermal-tempering analysis of bulk metallic glass plates using an instant-freezing model," *Metallurgical and Materials Transactions A,* vol. 32, pp. 2709-2715, 2001.
[83] V. I. Tkatch, A. I. Limanovskii, S. N. Denisenko, and S. G. Rassolov, "The effect of the melt-spinning processing parameters on the rate of cooling," *Materials Science and Engineering: A,* vol. 323, pp. 91-96, 2002.
[84] V. A. Pozdnyakov, O. V. Borisov, and V. P. Filippova1, "Simulating Residual Stresses in Ribbons of Amorphous Metallic Alloys," *Journal of ASTM International,* vol. 7, 2010.

[85] M. Calvo-Dahlborg, "Structure and embrittlement of metallic glasses," *Materials Science and Engineering: A,* vol. 226–228, pp. 833-845, 1997.
[86] A. Lovas, E. Kisdi-Koszó, L. Potocký, and L. Novák, "Effect of processing conditions on physical properties of transition metal-metalloid metallic glasses," *Journal of Materials Science,* vol. 22, pp. 1535-1546, 1987/05/01 1987.
[87] S.-C. Huang and H. Fiedler, "Effects of Wheel Surface Conditions on the Casting of Amorphous Metal Ribbons," *Metallurgical Transactions A,* vol. 12, pp. 1107-1112, 1981/06/01 1981.
[88] F. Varret, G. Gal, and M. Henry, "The curvature of amorphous metallic ribbons interpreted with a homogeneous quenching model," *Journal of Materials Science,* vol. 24, pp. 3399-3402, 1989/09/01 1989.
[89] F. O. Méar, G. Vaughan, A. R. Yavari, and A. L. Greer, "Residual-stress distribution in shot-peened metallic-glass plate," *Philosophical Magazine Letters,* vol. 88, pp. 757-766, 2008/11/01 2008.
[90] F. O. Méar, B. Lenk, Y. Zhang, and A. L. Greer, "Structural relaxation in a heavily cold-worked metallic glass," *Scripta Materialia,* vol. 59, pp. 1243-1246, 2008.
[91] C. Jeon, C. Son, C. Kim, and S. Lee, "Effects of Shot Peening on Fatigue Properties of Zr-based Amorphous Alloys Containing Ductile Crystalline Particles," *Metallurgical and Materials Transactions A,* vol. 43, pp. 471-478, 2012/02/01 2012.
[92] A. Concustell, F. O. Méar, S. Suriñach, M. D. Baró, and A. L. Greer, "Structural relaxation and rejuvenation in a metallic glass induced by shot-peening," *Philosophical Magazine Letters,* vol. 89, pp. 831-840, 2009/12/01 2009.
[93] G. Chen, H. Bei, Y. Cao, A. Gali, C. T. Liu, and E. P. George, "Enhanced plasticity in a Zr-based bulk metallic glass composite with in situ formed intermetallic phases," *Applied Physics Letters,* vol. 95, 2009.
[94] C. C. Hays, C. P. Kim, and W. L. Johnson, "Microstructure Controlled Shear Band Pattern Formation and Enhanced Plasticity of Bulk Metallic Glasses Containing *in situ* Formed Ductile Phase Dendrite Dispersions," *Physical Review Letters,* vol. 84, pp. 2901-2904, 03/27/ 2000.
[95] G. Y. Sun, G. Chen, and G. L. Chen, "Design, synthesis, and characterization of bulk metallic glass composite with enhanced plasticity," *Journal of Materials Science,* vol. 46, pp. 5216-5220, 2011/08/01 2011.
[96] G. He, J. Eckert, W. Loser, and L. Schultz, "Novel Ti-base nanostructure-dendrite composite with enhanced plasticity," *Nat Mater,* vol. 2, pp. 33-7, Jan 2003.
[97] B. Sarac and J. Schroers, "Designing tensile ductility in metallic glasses," *Nat Commun,* vol. 4, 07/17/online 2013.
[98] C. C. Aydıner, E. Üstündag, B. Clausen, J. C. Hanan, R. A. Winholtz, M. A. M. Bourke*, et al.*, "Residual stresses in a bulk metallic glass–stainless steel composite," *Materials Science and Engineering: A,* vol. 399, pp. 107-113, 2005.
[99] Y. J. Liu, I. T. H. Chang, and M. R. Lees, "Influences of oxide phases on the coercivity of mechanically alloyed multicomponent Fe-based amorphous alloys," *Scripta Materialia,* vol. 44, pp. 2729-2734, 6/8/ 2001.
[100] R. O. Ritchie, V. Schroeder, and C. J. Gilbert, "Fracture, fatigue and environmentally-assisted failure of a Zr-based bulk amorphous metal," *Intermetallics,* vol. 8, pp. 469-475, 5// 2000.

[101] F. X. Liu, Y. F. Gao, and P. K. Liaw, "Rate-Dependent Deformation Behavior of Zr-Based Metallic-Glass Coatings Examined by Nanoindentation," *Metallurgical and Materials Transactions A,* vol. 39, pp. 1862-1867, 2008/08/01 2008.
[102] V. M. Sglavo, M. Bonafini, and A. Prezzi, "Procedure for residual stress profile determination by curvature measurements," *Mechanics of Materials,* vol. 37, pp. 887-898, 8// 2005.
[103] A. Concustell, F. O. Mear, S. Surinach, M. D. Baro, and A. L. Greer, "Structural relaxation and rejuvenation in a metallic glass induced by shot-peening," *Philosophical Magazine Letters,* vol. 89, pp. 831-840, // 2009.
[104] L. M. Wang, W. H. Wang, R. J. Wang, Z. J. Zhan, D. Y. Dai, L. L. Sun*, et al.*, "Ultrasonic investigation of $Pd_{39}Ni_{10}Cu_{30}P_{21}$ bulk metallic glass upon crystallization," *Applied Physics Letters,* vol. 77, pp. 1147-1149, 2000.
[105] D. Deng and B. Lu, "Density change of glassy $Pd_{77}Si_{16.5}Cu_{6.5}$ alloy during cold drawing," *Scripta Metallurgica,* vol. 17, pp. 515-518, 4// 1983.
[106] U. Harms, O. Jin, and R. B. Schwarz, "Effects of plastic deformation on the elastic modulus and density of bulk amorphous $Pd_{40}Ni_{10}Cu_{30}P_{20}$," *Journal of Non-Crystalline Solids,* vol. 317, pp. 200-205, 3// 2003.
[107] M. Miller and P. Liaw, *Bulk Metallic Glasses*: Springer US, 2008.
[108] Y. Suzuki, J. Haimovich, and T. Egami, "Bond-orientational anisotropy in metallic glasses observed by x-ray diffraction," *Physical Review B,* vol. 35, pp. 2162-2168, 02/15/ 1987.
[109] F. Abdeljawad, M. Fontus, and M. Haataja, "Ductility of bulk metallic glass composites: Microstructural effects," *Applied Physics Letters,* vol. 98, p. 031909, 2011.
[110] J. Hee-Won, S. Hata, and A. Shimokohbe, "Microforming of three-dimensional microstructures from thin-film metallic glass," *Microelectromechanical Systems, Journal of,* vol. 12, pp. 42-52, 2003.

VITA

Balaji Jayakumar

Candidate for the Degree of

Doctor of Philosophy

Thesis: MECHANICAL PROPERTIES OF A NEW HIGH SPECIFIC STRENGTH HONEYCOMB FROM AMORPHOUS METAL

Major Field: Mechanical and Aerospace Engineering

Biographical:

Education:

Completed the requirements for the Doctor of Philosophy in Mechanical and Aerospace Engineering at Oklahoma State University, Stillwater, Oklahoma in December, 2014.

Completed the requirements for the Master of Science in Mechanical and Aerospace Engineering at Oklahoma State University, Stillwater, Oklahoma in December, 2009.

Completed the requirements for the Bachelor of Engineering in Aeronautical Engineering at Anna University, Chennai, India in 2006.

Experience:

Graduate Research Assistant (January 2008- February 2015)
Hanan research lab. Oklahoma State University.

Graduate Teaching Assistant (August 2007 – May 2012)
Mechanical and Aerospace Engineering, Oklahoma State University.

Graduate Assistant to Lab Manager (August 2008 – December 2009)
Material Science and Metallurgy labs, Oklahoma State University, Tulsa.